Hydrogen self-dynamics in liquid H_2-D_2 mixtures studied through inelastic neutron scattering

Daniele Colognesi,[1,*] Ubaldo Bafile,[1] Milva Celli,[1] Martin Neumann,[2] and Andrea Orecchini[3,4]

[1]*Consiglio Nazionale delle Ricerche, Istituto dei Sistemi Complessi, via Madonna del Piano 10, I-50019 Sesto Fiorentino, Italy*

[2]*Fakultät für Physik der Universität Wien, Strudlhofgasse 4, A-1090 Wien, Austria*

[3]*Physics and Geology Department, University of Perugia, Via Pascoli, I-06123 Perugia, Italy*

[4]*Institut Laue-Langevin, 71 av. des Martyrs, F-38042 Grenoble Cedex 9, France*

(Received 9 April 2015; revised manuscript received 25 May 2015; published 15 July 2015)

We have measured the dynamic structure factor of liquid para-hydrogen mixed with normal deuterium (T = 20 K) at two different concentration levels using incoherent inelastic neutron scattering. This choice has been made since the presence of D_2 modifies the self-dynamics of H_2 in a highly nontrivial way, acting both on its pseudophononic and its diffusive parts in a tunable way. After an accurate data reduction, recorded neutron spectra were studied through the modified Young and Koppel model and the H_2 center-of-mass self-dynamics structure factor was finally extracted for the two mixtures. Some physical quantities (i.e., self-diffusion coefficient and mean kinetic energy) were determined and compared with accurate quantum calculations, which, in addition, also provided estimates of the velocity autocorrelation function for the H_2 centers of mass. These estimates, in conjunction with the Gaussian approximation, were used to simulate the H_2 center-of-mass self-dynamics structure factor in the same range as the experimental one. The agreement between measured and calculated spectra was globally good, but some discrepancies proved the unquestionable breakdown of the Gaussian approximation in these semiquantum systems at a level comparable to that already observed in pure liquid para-hydrogen.

DOI: 10.1103/PhysRevE.92.012311 PACS number(s): 66.10.cg, 61.05.fg, 67.10.Hk

I. INTRODUCTION

Understanding the microscopic dynamics of liquid systems exhibiting moderate quantum effects (a.k.a. *semiquantum liquids*), such as ^{4}He above the λ transition, ^{3}He warmer than its Fermi temperature, molecular hydrogen, deuterium and tritium, neon, and their various mixtures, is still one of the open problems in condensed matter physics [1]. In general, semiquantum liquids are systems that are fluid at a temperature lower than their Debye temperature [2]. However, differently from the highly quantum fluids (e.g., superfluid ^{4}He and degenerate liquid ^{3}He), the corresponding quantum statistics (Bose-Einstein or Fermi-Dirac) seems to play no significant role in the translational dynamics of the particles composing semiquantum liquids [2], so that it is sensible to apply the Maxwell-Boltzmann statistics to describe most of their properties.

Several theoretical approaches to the semiquantum liquid dynamics have been tried in the past, but, despite some interesting results, none of them has come out as thoroughly satisfactory. On the computational side, centroid molecular dynamics (CMD) [3] and ring polymer molecular dynamics (RPMD) [4] are surely the simulation techniques producing the best results for semiquantum liquids, but their scope is limited to evaluate the time-correlation functions of operators linear in **r** or **p** only. The *Feynman-Kleinert linearized path integral* does not seem to suffer these limitations [5], but its capability to precisely reproduce the dynamic structure factors of liquid hydrogen and deuterium is still a matter of discussion [6]. Given this scenario, any precise experimental determination of dynamic quantities (i.e., time-correlation functions or their frequency spectra) that can be compared to corresponding theoretical predictions becomes highly valuable, like, for instance, a recent experiment on pure liquid H_2 [7,8]. In this study, we now aim to obtain experimental results on the microscopic single-particle dynamics of para-hydrogen (p-H_2) in its liquid mixtures with normal deuterium (n-D_2). This hydrogen-based liquid system has been selected for two reasons: first because of the clear and evident semiquantum character of its components, which has attracted a number of theoretical studies, simulations, and experimental works [9] and second because of the peculiar molecular hydrogen properties when H_2 is interacting with thermal neutrons. [As explained in detail in the literature [10], it is possible to single out the self-dynamics of the p-H_2 molecular center of mass (c.m.) in a condensed system by means of inelastic neutron scattering.] In other words, the neutron scattering double-differential cross section of a collection of p-H_2 molecules can be easily related to the self-part of the c.m. dynamic structure factor $S_{s,\mathrm{c.m.}}(Q,E)$ (with Q and E being the wave-vector and energy transfers, respectively), which is an intrinsic physical property of the hydrogen-containing system under investigation related to the single molecule dynamics. At this stage, it is a common practice to try to connect $S_{s,\mathrm{c.m.}}(Q,E)$ to the power spectrum of the velocity autocorrelation function (VACF). Whenever $S_{s,\mathrm{c.m.}}(Q,E)$ is not available in a wide Q range so that a low Q extrapolation becomes possible, this connection is attempted by means of the well-known Gaussian approximation (GA) [11]. This approximation has been proved to be exact in some simple model systems: a perfect gas, a harmonic solid, and a fluid in which the particle movements are governed by the Langevin equation. Even though it has been found by some neutron scattering experiments [12] and simulations on classical fluid argon that there exist areas of the (Q,E) kinematic plane in which the GA does not hold precisely, the latter is still widely used, and no complete critical assessment about its validity has been undertaken, especially

*Corresponding author: daniele.colognesi@isc.cnr.it

in connection with semiquantum liquids. In this respect, the mentioned work on pure liquid p-H_2 [7,8] was able to detect clear experimental evidences of a deviation from the GA four times larger than in liquid Ar (see Fig. 3 in Ref. [7]), probably due to the more quantum nature of the former system. Thus, the purpose of this study is to investigate the GA when applied to p-H_2 mixtures with deuterium: here the quantum character of H_2 is stronger than in the pure liquid hydrogen, as shown by comparing the respective zero-point c.m. mean kinetic energy values [13], which are dominated by the pseudophononic dynamics of the system. In addition, one observes a lower value of the H_2 self-diffusion coefficient D_s since the diffusive motion of H_2 is hindered by an increased density and, possibly, by the formation of short-lived D_2 cages around the molecule [13]. Summarizing, this study aims to represent a significant step forward in the knowledge on the applicability range and the limits of the GA since the presence of D_2 modifies the self-dynamics of H_2 in a highly nontrivial way, acting on both its pseudophononic and its diffusive parts in a tunable way.

The rest of this paper will be organized as follows: The experimental procedure will be described in detail in Sec. II, while in Sec. III we will work out the self-dynamics structure factor of liquid para-hydrogen starting from the experimental neutron spectra. Section IV will be fully devoted to the computational details concerning the quantum dynamics simulations performed on the H_2-D_2 mixtures under investigation, in order to extract their VACF's. In Sec. V, we will discuss the obtained results and we will check the validity of the GA: the physical quantities derived from the experimental spectra will be compared to their estimates obtained from the aforementioned quantum simulations. Section VI will be finally devoted to conclusions and perspectives.

II. EXPERIMENTAL DETAILS

Neutron scattering measurements were carried out on IN4C, a spectrometer located at the Institut Laue-Langevin (Grenoble, France). IN4C [14] is a so-called hybrid-geometry spectrometer, where a crystal monochromator fixes the initial neutron energy, and a chopper system determines the final neutron energy by time-of-flight (TOF) analysis. The thermal neutron beam emerging from the reactor is first collimated (divergence, 1°) before impinging, with a Bragg angle varying between 19° and 32°, on the double focusing monochromator [15]. In the case of our experiment, the selected value of incoming neutron wavelength was $\lambda_0 = 1.153$ Å from the (006) Bragg reflection of an array of highly oriented pyrolytic graphite crystals. This corresponds to an incoming neutron energy $E_0 = 61.521$ meV. Two rotating disk choppers, upstream the monochromator, are used both to suppress contaminations from higher-order monochromator reflections and to minimize the background produced by thermal neutrons and gamma rays coming from the moderator. The beam is finally reduced to short pulses by a Fermi chopper and hits the sample after passing through another collimating diaphragm. Neutrons scattered by the sample are then collected by 300 ^{3}He tubes covering angles from 13° up to 120°. In addition, a ^{3}He-filled multidetector allows to observe forward scattering from 8.7° down to an angle of about 2.4°.

TABLE I. Thermodynamic conditions of the measured liquid samples, including sample number, species, temperature T, hydrogen concentration $c[H_2]$, pressure p, total molecular density n, and counting time t.

No.	Species	T (K)	$c[H_2]$ (%)	p (mbar)	n (nm^{-3})	t (s)
(1)	Vanadium	100.00(1)				8883
(2)	Empty can	20.7(2)				43090
(3)	Pure D_2	20.26(4)	0.0	358.3(4)	25.52(4)	58008
(4)	H_2-D_2	20.22(1)	24(2)	600(30)	24.4(1)	50400
(5)	H_2-D_2	20.26(2)	50(1)	759(6)	23.24(5)	46180

A comprehensive description of the samples (including species, temperature, hydrogen concentration, pressure, total molecular density, and counting time) can be found in Table I. As far as the total molecular density is concerned, the reported estimates were obtained from reliable thermodynamic data available in the literature: Ref. [16] for pure hydrogen, Ref. [17] for pure deuterium, and Ref. [18] for hydrogen-deuterium mixtures. Another important issue is the rotational population of the hydrogen (and deuterium, to a lesser extent) molecules composing the experimental samples: as it will be made clear later in this section, equilibrium hydrogen (e-H_2) has been always employed. This is hydrogen in which the ortho-para distribution is in thermodynamic equilibrium at the actual temperature of the sample. In this respect, considering the temperature values reported in Table I, one can assume for the two mixture samples to deal only with para-hydrogen species since at $T = 20$ K, the para-hydrogen concentration is very high: $c[\mathrm{p}-\mathrm{H_2}]/c[\mathrm{e}-\mathrm{H_2}] = 99.821\%$ [16]. On the contrary, normal deuterium (n-D_2) has been used for preparing both the pure D_2 sample and the two mixture ones. It exhibits a concentration of the ortho-deuterium (o-D_2) which can be estimated to be around $c[\mathrm{o}-\mathrm{D_2}]/c[\mathrm{n}-\mathrm{D_2}] = 66.7\%$, i.e., identical to the room temperature case. The choice to employ $\mathrm{n}-\mathrm{D_2}$ instead of pure o-D_2 was dictated by experimental reasons and is justified by the modest differences in the liquid-deuterium neutron cross section in the two cases.

After performing a calibration measurement at $T = 100$ K making use of an appropriate vanadium rod (43.0 mm long, 15.0 mm diameter), we inserted the sample container (i.e., the scattering cell) into the instrumental sample chamber equipped with an Orange cryostat, we cooled it down to the desired temperature (about $T = 20$ K), and then we measured the cell neutron spectrum for a counting time of about 12 h dividing this run into six subruns. The cell was made of aluminum with a circular-slab geometry (annulus) and consisted in two concentric cylinders giving rise to a 1.0-mm void to be filled with the liquid sample, exhibiting an average diameter of 15.0 mm. The external diameter of the container was 20.0 mm coinciding with the horizontal beam size (about 20 mm, including penumbra). The container total height (75.0 mm) was rather bigger than the vertical beam size (about 60 mm, including penumbra), so the cell was masked with cadmium wraps in order to exclude its bulky ends which contained no liquid sample (the annulus vertical size being only 55 mm). In this way the portion of cell irradiated by neutrons was reduced

to 43 mm, identical to the length of the vanadium rod used for calibration purposes.

Subsequently, the temperature of the cell was increased to $T = 23$ K and normal deuterium gas (*air liquide*, 99.9% assay) was allowed to condense in it. The pressure of the gas handling system was initially set to $p = 900$ mbar (slightly larger than the corresponding saturated vapor pressure, SVP = 834.44 mbar [17]). Then, the cell temperature was slowly decreased (in order to prevent the formation of solid plugs in the tubes) to $T = 4$ K where the pressure reached the final value of $p = 0.97$ mbar and n-D_2 froze in the sample container. At this stage, knowing the exact initial volume of the D_2 gas in the handling system, we were sure that the cell was completely filled with the sample. Later on, the temperature was raised again to 20 K and a neutron measurement (divided into nine subruns) was started, lasting for about 16 h. The stability of the thermodynamic conditions during this measurement was satisfactory: the temperature and pressure uncertainties were estimated to be around 0.04 K and 0.4 mbar, respectively.

As for the mixture samples Nos. (4) and (5) (see Table I), they were obtained in a different and more elaborate way. Let us summarize the main steps of the procedure followed to produce the former liquid H_2-D_2 mixture [i.e., sample No. (4) with $c[H_2] = 24\%$], recalling that the latter was prepared similarly. The first part of mixture preparation was the off-line production of liquid p-H_2 by means of an external conversion cell (volume: 23.5 cm^3) filled with liquid hydrogen (*alpha gas*, 99.999% assay) and left at temperatures cycling between 15 and 19 K for 24 h. At the bottom of the conversion cell some powder of a paramagnetic catalyst, made of Cr_2O_3 on an Al_2O_3 substrate, had been inserted in order to speed up the conversion from ortho- to para-hydrogen. Then, gaseous para-hydrogen was produced boiling off the liquid at $T = 26$ K and then mixed with normal deuterium in a buffer volume at room temperature under a total pressure of about 3 bar. The exact amount of gaseous mixture needed to fill up the sample cell (identical to the can already used for pure n-D_2) with the corresponding liquid was condensed in it at $T = 20$ K. Then, the cell was slowly cooled down to $T = 2$ K, so to decrease the vapor pressure of the gas handling line to an extremely low value: 1.37 mbar. This step was regarded as very important in order to prevent an undesired separation of the mixture [19], where the more volatile gas (i.e., H_2) could concentrate in the buffer volume, while the less volatile (i.e., D_2) condensed in coldest point of the gas line, namely, the sample cell. This would have altered the mixture composition in quite a noticeable way. At the end, the sample can was isolated from the rest of the gas handling line and warmed up to the requested experimental temperature (20 K). It is worth noting that the mixture was prepared on a time scale of few hours, surely too short to alter the $c[p-H_2]/c[e-H_2]$ and $c[o-D_2]/c[n-D_2]$ ratios in absence of specific paramagnetic catalysts. It was estimated (see next section for details) that the present geometry of the selected liquid mixtures gave rise to a total scattering of 12.3%, 18.2%, and 23.8% of the incoming neutron beam for samples Nos. (3), (4), and (5), respectively. The corresponding single scattering values were evaluated to be 11.5%, 16.4%, and 20.7%.

III. DATA ANALYSIS

At the end of our neutron scattering experiment on IN4C, time-of-flight data recorded by each single detector bank were normalized to the incoming neutron counts of the monitor, purged of noisy tubes, corrected for detector efficiency, and binned into 188 angular intervals, ranging from $\theta = 13.1^\circ$ to 120.3°. Subsequently, processed time-of-flight data were automatically subtracted of the flat fast neutron background and then transformed into energy-transfer (E) spectra, correcting for the well-known kinematic factor $\sqrt{(E_0 - E)/E_0}$ [20]. These new data sets exhibited energy-transfer values up to 56.1 meV. Finally, the usual vanadium spectra normalization was operated, taking into account the minute angular effect due to the Debye-Waller factor of this metal. Neutron data (now transformed into the E domain and plotted in Fig. 1 for a selected example at $\theta = 23.43^\circ$) exhibited an average resolution $\Delta E = 3.52$ meV at the elastic line. This resolution figure turned out to be only slightly increasing with θ (e.g., from 3.23 meV at $\theta = 13.07^\circ$ to 3.85 meV at $\theta = 120.12^\circ$), as it was derived from the mentioned vanadium rod calibration measurements. As for the ΔE variation with E (keeping θ fixed), we relied on the instrumental routines [21] which pointed out (for the present instrumental configuration) a rapid decrease of ΔE down to a minimum placed at $E = 12.32$ meV, where ΔE is reduced to 74.7% of its elastic line value, followed by a neat increase so that the elastic line value is quickly regained at $E = 27.91$ meV. Finally, at $E = 54.30$ meV, ΔE amounts to 168.9% of the vanadium estimate.

The outputs of this part of the data analysis procedure are the so-called $\Sigma(\theta, E)$ spectra, particularly suitable for the following operations:

(a) empty can scattering subtraction after considering sample attenuation;

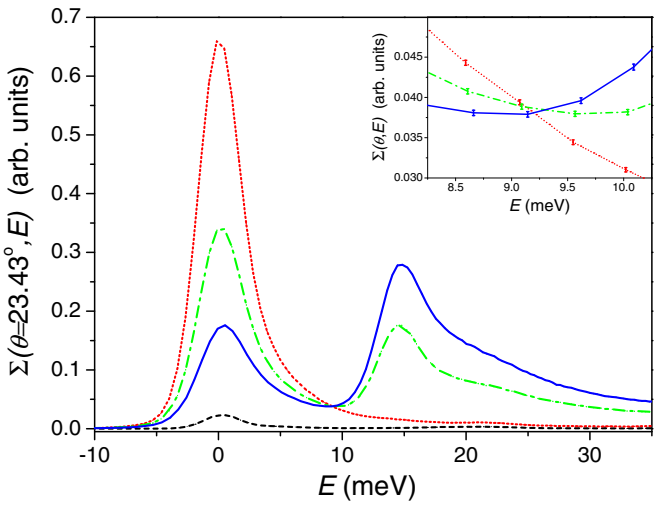

FIG. 1. (Color online) Main panel: experimental raw spectral data as in Table I, corrected for the kinematic factor, in the angular range $21.83^\circ < \theta < 25.92^\circ$ (average value: $\theta = 23.43^\circ$). The empty can spectrum is plotted as a dashed black line and the pure liquid D_2 one as a dotted red line, while the dotted-dashed green line and the full blue line represent the two H_2-D_2 mixtures at $c[H_2] = 24\%$ and 50%, respectively. Inset: same data as in the main panel, but zoomed to show the experimental statistical accuracy.

(b) sample self-shielding evaluation and correction;

(c) multiple scattering evaluation, simulation, and subtraction.

Points (a) and (b) were implemented using a Monte Carlo routine which simulated the scattering cell in the two conditions: empty and filled with the various samples. In these simulations, no simplified model was employed for the normal deuterium total scattering cross section $\sigma_{t,\text{n-D}_2}(E_0)$, which, on the contrary, was obtained from the experimental results of direct measurements on liquid n-D_2 at $T = 19$ K up to $E_0 = 78.2$ meV [22]. As for the total cross section of the H_2-D_2 mixtures, a proper linear combination of the aforementioned quantity $\sigma_{t,\text{n-D}_2}(E_0)$ with the total scattering cross sections of liquid para-hydrogen at $T = 16$ K [22] $\sigma_{t,\text{p-H}_2}(E_0)$, was assumed to be accurate enough for the self-attenuation correction.

As for point (c), multiple scattering spectra were accurately simulated through the analytical approach suggested by Agrawal and Sears [23], in conjunction with the Vineyard approximation [20], the well-known modified Young-Koppel model for both H_2 and D_2 [10,24], and the GA for the molecular c.m. dynamics [11]. Following the various tasks of the calculation we can sketch the entire multiple scattering evaluation procedure in three main steps:

(c-i) Using model VACF's for the D_2 and H_2 centers of mass to generate the respective center-of-mass self-scattering laws in an appropriate portion of the kinematic plane (Q,E) through the mentioned Gaussian approximation. It has been verified that the following rectangular zone was sufficiently large for our purpose: $0.1\,\text{Å}^{-1} < Q < 12\,\text{Å}^{-1}$, $-16\,\text{meV} < E < 80\,\text{meV}$.

(c-ii) Applying the modified Young-Koppel model to transform the self c.m. scattering laws into double-differential cross section including the rotational dynamics of both D_2 and H_2 through appropriate convolutions. The first eight rotational levels of D_2 and H_2 (labeled by j'), $0 \leqslant j' \leqslant 7$, have been considered in this calculation.

(c-iii) Implementing the cited formulas by Sears [23] in the case of an annulus, making use of the energy-dependent self-attenuation factors already evaluated in points (a) and (b). This final step has been accomplished through a Monte Carlo code since the analytical approach was too demanding for a complex geometry like that of our scattering cell (see previous section for the cell details).

To sum up, the only needed input data were the VACF's for liquid D_2 and H_2-D_2 mixtures as in Table I, which have been taken from the quantum simulations reported in Sec. IV. The stability of the multiple scattering simulation results was checked by replacing the GA-simulated self center-of-mass scattering laws with their coarser versions obtained via a quantum version of the simple Egelstaff-Schofield model [25] (see Appendix A for details). Visible changes were observed in the single scattering spectra, but no detectable discrepancy was present in the multiple scattering ones.

At this stage, $\Sigma(\theta,E)$ spectra were transformed into constant-Q data, $\Sigma(Q,E)$, through interpolation routines. This transformation made possible the determination of inelastic spectra at Q values approximately ranging in the interval $1.4\,\text{Å}^{-1} < Q < 8.0\,\text{Å}^{-1}$ in steps of $0.2\,\text{Å}^{-1}$.

The following move of the data reduction procedure included the subtraction of the scattering due to deuterium from the spectra of samples Nos. (4) and (5). This was accomplished making use of the experimental pure deuterium spectrum [i.e., sample No. (3)], properly scaled to account for sample molecular densities and D_2 concentrations. A detailed justification of this operation in the case of inelastic neutron scattering from liquid H_2-D_2 mixtures can be found in Ref. [13]. After this subtraction, processed neutron spectroscopic data contained only scattering from p-H_2 and so could be dubbed as $\Sigma_{\text{p-H}_2}(Q,E)$. In the aforementioned reference it is also shown that in the present energy transfer range $\Sigma_{\text{p-H}_2}(Q,E)$ contains only one relevant rotational term, which is related to the $j = 0 \rightarrow j' = 1$ hydrogen transition. Under this important assumption one can extract the self-part of the c.m. dynamic structure factor $S_{s,\text{c.m.}}(Q,E)$ making use of the cited modified Young-Koppel model [10]:

$$\Sigma_{\text{p-H}_2}(Q,E) = \frac{\sigma_{0-1}}{4\pi} j_1^2(Qd/2)\exp[-2W_v(Q)]S_{s,\text{c.m.}}(Q,E) \times \otimes \delta(E - E_{0-1}), \quad (1)$$

where $\sigma_{0-1} = 4 \times 80.26$ barn [20,26] is the neutron cross section for the $j = 0 \rightarrow j' = 1$ rotational transition in H_2, $j_n(x)$ is a spherical Bessel function of the first kind, d is the internuclear distance in the H_2 molecule (i.e., $d = 0.742$ Å [27]), $W_v(Q)$ is the exponent of the Debye-Waller factor due only to the H_2 intramolecular vibration [24] (totally negligible in the present Q range), and E_{0-1} is the energy shift due to the $j = 0 \rightarrow j' = 1$ rotational transition in H_2 (i.e., $E_{0-1} = 14.7$ meV [27]). The experimental estimates of the self-part of the p-H_2 c.m. dynamic structure factor $S_{s,\text{c.m.}}(Q,E)$ have been reported in Figs. 2 and 3 for samples Nos. (4) and (5), respectively.

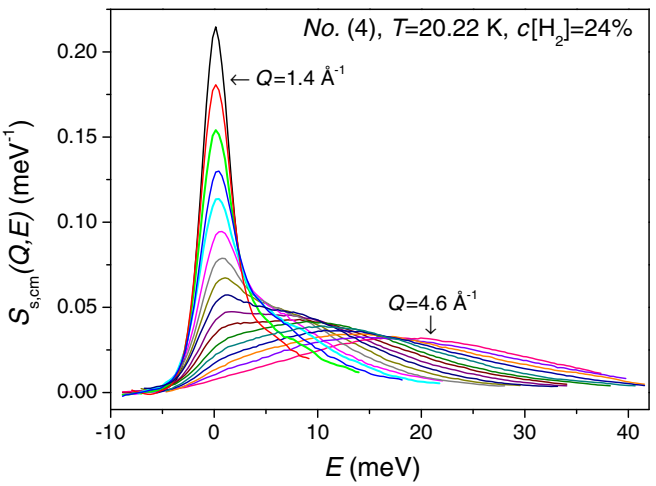

FIG. 2. (Color online) Experimental estimates of the self-part of the para-hydrogen center-of-mass dynamic structure factor $S_{s,\text{c.m.}}(Q,E)$, in the H_2-D_2 mixture sample No. (4) (i.e., $c[H_2] = 24\%$, see Table I) shown for Q values ranging from 1.4 Å^{-1} (black line, the most peaked and leftmost) to 4.6 Å^{-1} (pink line, the least peaked and rightmost).

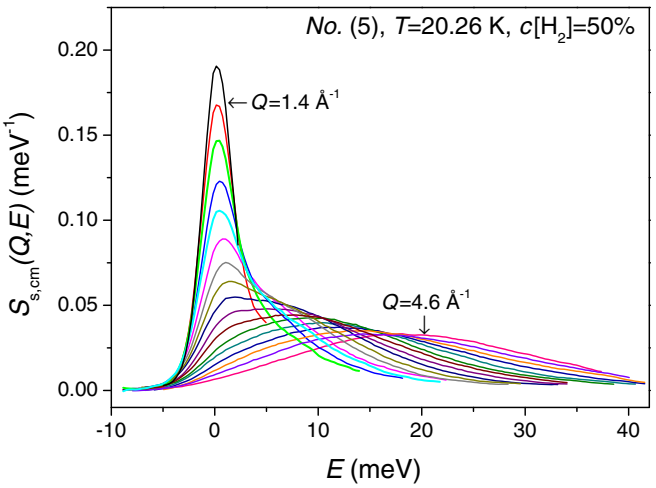

FIG. 3. (Color online) Experimental estimates of the self-part of the para-hydrogen center-of-mass dynamic structure factor $S_{s,\mathrm{c.m.}}(Q,E)$, in the H_2-D_2 mixture sample No. (5) (i.e., $c[H_2] = 50\%$, see Table I) shown for Q values ranging from 1.4 Å^{-1} (black line, the most peaked and leftmost) to 4.6 Å^{-1} (pink line, the least peaked and rightmost).

IV. QUANTUM DYNAMICS SIMULATIONS

In order to provide the H_2 VACF's required for the analysis of the experimental samples Nos. (3)–(5), as well as to extend the results theoretically to the entire concentration range, we have performed a series of CMD simulations. In these simulations, all interactions were modeled by the spherically symmetric Silvera-Goldman potential [28], the only difference between H_2 and D_2 being the molecular mass $2m_{\mathrm{H}} = 2.016$ amu versus $2m_{\mathrm{D}} = 4.028$ amu. The total number of molecules was always $N = N[H_2] + N[D_2] = 256$, and the H_2 concentrations of the 14 thermodynamic states listed in Table II were realized by assigning the lighter mass to $N[H_2]$ of the particles and the heavier mass to the remaining ones. Since CMD is basically a classical molecular dynamics technique in a quantum mechanical force field, we have calculated these forces by very short path integral Monte Carlo (PIMC) simulations at each time step, using the primitive algorithm and a Trotter number of $P = 64$ for the number of beads on the classical ring polymers replacing the quantum particles in PIMC. Although more time consuming than the usual implementation, this avoids sampling problems due to the stiff internal modes of the polymers and allowed us to use a time step $\Delta t = 0.005$ ps. The classical dynamics was kept at a temperature $T = 20$ K by means of a Gaussian thermostat [29], and the overall molecular densities (n) of the mixtures were taken from Refs. [16–18]. At each thermodynamic state we have performed 10 independent runs of 10^5 time steps (500 ps) each, in order to get an estimate of the statistical uncertainty of the results. The VACFs were calculated up to a maximum time lag of 2.5 ps and multiplied by a Welsh window [30] before Fourier transforming. Since a CMD simulation yields the Kubo transform [31] $\langle \vec{v}(0)\cdot\vec{v}(t)\rangle^{(k)}_{\mathrm{D_2,H_2}}$ rather than the proper quantum mechanical VACF for the D_2 and H_2 c.m.'s, the spectral functions $f_{\mathrm{D_2,H_2}}(\omega)$ were obtained from the relationship

$$f_{\mathrm{D_2,H_2}}(\omega) = \frac{2m_{\mathrm{D,H}}}{3\pi k_B T}\int_{-\infty}^{\infty} \exp(-i\omega t)\langle \vec{v}(0)\cdot\vec{v}(t)\rangle^{(k)}_{\mathrm{D_2,H_2}} dt. \tag{2}$$

Examples of the results are reproduced in Fig. 4 for selected thermodynamic conditions, while a complete three-dimensional plot of the H_2 VACF as a function of both concentration $c[H_2]$ and time t is reported in Fig. 5. The latter shows an increment of the first dip (centered around $t = 0.2$ ps) as $c[H_2]$ gets smaller providing a clear illustration of physical fact that H_2 increasingly feels a caging effect when the deuterium concentration (and the molecular density) are raised.

TABLE II. Thermodynamic conditions of the liquid samples simulated at $T = 20.0$ K and computational results, including simulation number, number of H_2 molecules $N[H_2]$, hydrogen concentration $c[H_2]$, total molecular density n, center-of-mass self-diffusion coefficient D_s for H_2 and D_2, center-of-mass mean kinetic energy from path integral Monte Carlo steps $\langle E_k\rangle^P$ for H_2 and D_2, and center-of-mass mean kinetic energy from VACF spectra $\langle E_k\rangle^f$ for H_2 and D_2. See main text for details.

No.	$N[H_2]$	$c[H_2]$ (%)	n (nm^{-3})	$D_{s,\mathrm{H_2}}$ ($\text{Å}^2\,\text{ps}^{-1}$)	$D_{s,\mathrm{D_2}}$ ($\text{Å}^2\,\text{ps}^{-1}$)	$\langle E_k\rangle^P_{\mathrm{H_2}}$ (K)	$\langle E_k\rangle^P_{\mathrm{D_2}}$ (K)	$\langle E_k\rangle^f_{\mathrm{H_2}}$ (K)	$\langle E_k\rangle^f_{\mathrm{D_2}}$ (K)
(o)	256	100.0	21.24	0.850(1)		61.77(1)		60.45(1)	
(i)	230	89.84	21.79	0.764(1)	0.702(3)	63.27(1)	49.01(2)	61.99(1)	48.72(3)
(ii)	205	80.08	22.29	0.701(1)	0.650(2)	64.68(1)	49.87(1)	63.33(1)	49.53(2)
(iii)	179	69.92	22.79	0.638(1)	0.587(1)	66.06(1)	50.72(1)	64.79(1)	50.44(1)
(iv)	154	60.16	23.25	0.581(1)	0.542(1)	67.44(1)	51.58(1)	66.12(2)	51.29(1)
(v)	139	54.30	23.51	0.556(1)	0.518(1)	68.18(1)	52.06(1)	66.88(2)	51.77(2)
(vi)	128	50.00	23.70	0.535(1)	0.499(1)	68.76(1)	52.41(1)	67.44(3)	52.09(1)
(vii)	102	39.84	24.13	0.491(2)	0.461(1)	70.00(1)	53.21(1)	68.70(2)	52.91(1)
(viii)	84	32.81	24.42	0.467(2)	0.438(1)	70.89(2)	53.73(1)	69.55(4)	53.45(2)
(ix)	77	30.08	24.53	0.455(2)	0.427(1)	71.22(1)	53.92(1)	69.92(2)	53.65(1)
(x)	64	25.00	24.72	0.439(2)	0.413(1)	71.75(2)	54.26(1)	70.45(3)	54.00(1)
(xi)	51	19.92	24.91	0.423(1)	0.400(1)	72.32(2)	54.63(1)	71.01(3)	54.35(1)
(xii)	26	10.16	25.26	0.395(2)	0.375(1)	73.35(3)	55.27(1)	72.16(4)	55.04(1)
(xiii)	0	0.00	25.60		0.348(1)		55.90(1)		55.62(1)

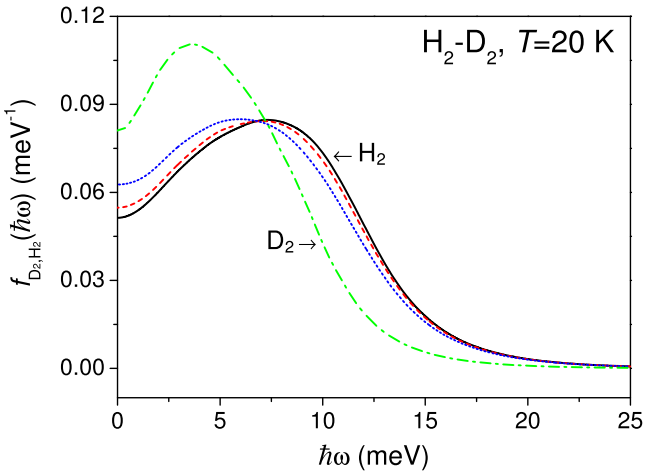

FIG. 4. (Color online) Simulations of the velocity autocorrelation function spectrum $f(\omega)$ for H_2 and D_2 centers of mass calculated in the thermodynamic conditions Nos. (vi), (viii), (x), and (xiii) (see Table II for details). H_2 spectra are plotted for Nos. (vi) (dotted blue line), (viii) (dashed red line), and (x) (full black line), i.e., for $c[H_2] = 50.0\%$, $c[H_2] = 32.8\%$, and $c[H_2] = 25.0\%$, respectively. A single D_2 spectrum is reported for No. (xiii) (dashed-dotted green line), which corresponds to the pure deuterium simulated sample.

One important piece of information contained in these spectra is the self-diffusion coefficient of the molecules, which is determined by the zero frequency value of $f_{D_2,H_2}(\omega)$:

$$D_{s,H_2} = \frac{\pi k_B T}{4m_H} f_{H_2}(0) = \frac{1}{3}\int_0^\infty \langle \vec{v}(0)\cdot\vec{v}(t)\rangle^{(k)}_{H_2} dt. \qquad (3)$$

Our CMD predictions for the self-diffusion coefficients for H_2 as well as for D_2 are included in Table II. Note that the uncertainties given there are merely the statistical errors and that the actual values may be slightly different since the self-diffusion coefficient is known to depend on system size [32]. For instance, from additional RPMD simulations of the equimolar mixture [i.e., No. (vi)] with $P = 64$, we find that the self-diffusion coefficient of H_2 changes from 0.496 to 0.507 $Å^2\ ps^{-1}$, and that of D_2 from 0.467 to 0.478 $Å^2\ ps^{-1}$, as the total number of molecules is increased from $N = 256$ to 500. On the other hand, varying, for the larger system, the Trotter number from $P = 32$ to 128, the self-diffusion coefficient of H_2 decreases from 0.517 to 0.496 $Å^2\ ps^{-1}$, and that of D_2 from 0.486 to 0.467 $Å^2\ ps^{-1}$. In the present context, potential corrections in the percent range are not important since we are primarily interested in the change of the self-diffusion coefficient with concentration. Another important and easily accessible physical quantity is the mean kinetic energy of the molecules' c.m., $\langle E_k\rangle_{D_2,H_2}$. Interestingly, there are two routes to this property in CMD. As in PIMC simulations, the mean kinetic energy may be calculated from the average potential energy stored in the "springs" of the polymers. Although this "crude energy estimator" [33] $\langle E_k\rangle^P_{D_2,H_2}$ is considered to be inferior to, e.g., the virial estimator [34], the statistical uncertainties are quite small in our case and probably smaller than the systematic error due to the finite Trotter number P. Alternatively, the mean kinetic energy may also be calculated from the spectral function $f_{D_2,H_2}(\omega)$ again [35]:

$$\langle E_k\rangle^f_{H_2} = \frac{3}{4}\hbar\int_0^\infty \omega\coth\left(\frac{\hbar\omega}{2k_BT}\right) f_{H_2}(\omega)d\omega. \qquad (4)$$

Obviously, this prediction is likewise affected by the finite value of P, but also by the overall quality of the simulated VACF and the specific way (such as windowing) in which $f_{D_2,H_2}(\omega)$ is calculated via Eq. (2). Both estimates of the kinetic energy are reported in Table II and should be contrasted to the value of 30 K for a classical system at $T = 20$ K. Finally, the GA expression [11] for the self-intermediate scattering function was applied to $f_{H_2}(\omega)$ in order to yield simulated neutron spectra. These, including the experimental energy resolution discussed in Sec. III, were dubbed $S^{(GA)}_{s,c.m.}$ and are reported in Figs. 6 and 7 for simulation Nos. (x) and

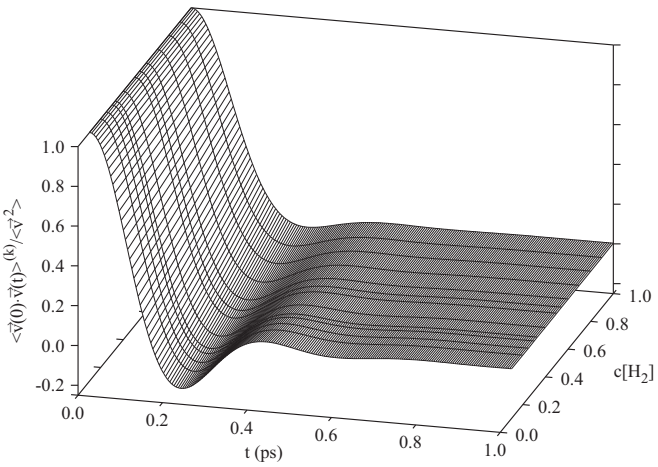

FIG. 5. Three-dimensional plot of the Kubo-transformed velocity autocorrelation functions $\langle\vec{v}(0)\cdot\vec{v}(t)\rangle^{(k)}$ for the H_2 centers of mass, simulated in the thermodynamic conditions Nos. (o)–(xii) (see Table II for details). For graphic reasons, data have been normalized making use of their $t = 0$ values $\langle\vec{v}^2\rangle$.

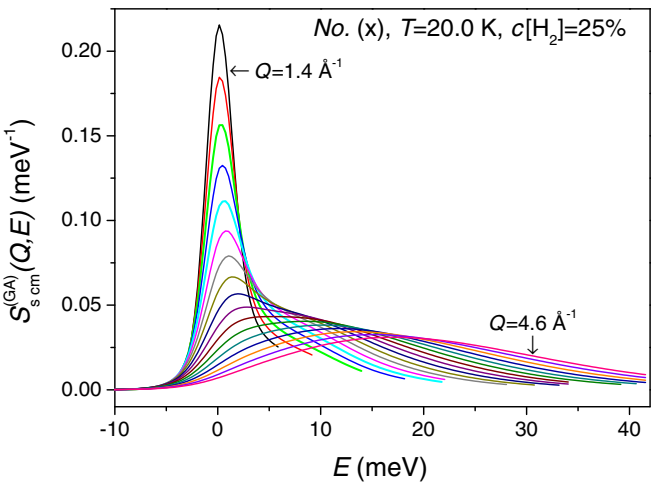

FIG. 6. (Color online) GA calculations of the self-part of the para-hydrogen center-of-mass dynamic structure factor $S^{(GA)}_{s,c.m.}(Q,E)$ in the H_2-D_2 mixture sample No. (x) (i.e., $c[H_2] = 25.0\%$, see Table II) shown for Q values ranging from 1.4 $Å^{-1}$ (black line, the most peaked and leftmost) to 4.6 $Å^{-1}$ (pink line, the least peaked and rightmost).

(vi), respectively. From now on, we will drop the subscript "H_2" from symbols like $f(\omega)$, D_s, and $\langle E_k \rangle$ to simplify the notation since we will be dealing with hydrogen only.

V. DISCUSSION

Although the original aim of the present experimental work was the study of the limits of the GA when applied to a semiquantum liquid mixture, from these measurements it is also possible to extract interesting and original information on other physical properties of the systems under investigation. As a matter of fact, to the authors' knowledge there are really few experimental spectroscopic data in the literature comparable with the present ones. Given this scenario, we have inspected Figs. 2 and 3 and starting from the following qualitative observations, we have tried to obtain a better understanding of some significant physical properties of these semiquantum liquid mixtures:

(a) The Q range explored is large enough to describe a complete and continuous change of the self-c.m. dynamics, spanning from a clearly diffusional regime at low values of momentum transfer (say, for $Q \leqslant 2.4\,\text{Å}^{-1}$) to an almost free-particle behavior at high Q values (say, for $Q \geqslant 3.6\,\text{Å}^{-1}$). In the middle, there is an interesting crossover where no simplified physical picture seems indeed possible.

(b) The H_2 c.m. spectral sets reported in the two aforementioned figures are quite similar, but not identical, proving that the density and concentration effects on the H_2-D_2 mixtures are indeed detectable by inelastic neutron scattering. In particular, the spectra collected at the lowest-Q values exhibit rather different values of peak widths.

Continuing with a quick check of the results, if now Figs. 6 and 7 are also considered, one can add a further preliminary conclusion:

(c) The use of the GA in conjunction with the VACF spectra derived from appropriate quantum calculations are able to describe, at least at a qualitative level, the experimental H_2 c.m. neutron spectra in their full (Q,E) double range.

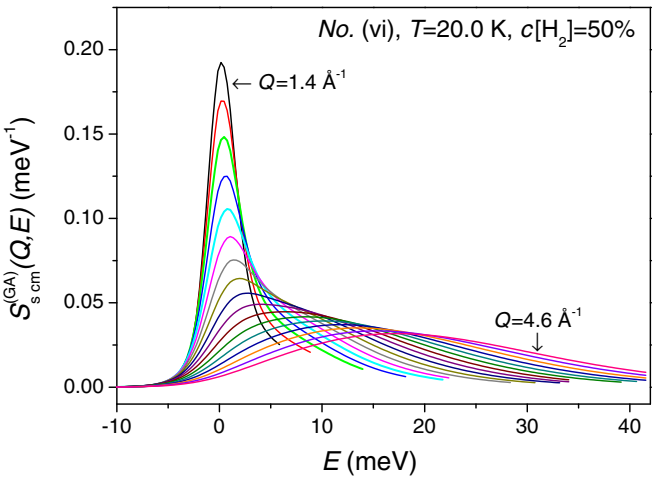

FIG. 7. (Color online) GA calculations of the self-part of the para-hydrogen center-of-mass dynamic structure factor $S^{(\mathrm{GA})}_{s,\mathrm{c.m.}}(Q,E)$ in the H_2-D_2 mixture sample No. (vi) (i.e., $c[H_2] = 50.0\%$, see Table II) shown for Q values ranging from 1.4 Å^{-1} (black line, the most peaked and leftmost) to 4.6 Å^{-1} (pink line, the least peaked and rightmost).

Thus, the rest of the present discussion will be developed along the lines sketched in the three points above, trying (a) to understand the mentioned crossover regime in the self-dynamics structure factor of the H_2 c.m.'s in order to obtain a physical picture of the interplay between single-particle diffusion, cage rattling, and pseudophonons [36]; (b) to extract from the experimental spectra [i.e., $S_{s,\mathrm{c.m.}}(Q,E)$] relevant physical quantities which could be sensitive to the differences existing between the two liquid samples; (c) to compare experimental $S_{s,\mathrm{c.m.}}(Q,E)$ with simulated $S^{(\mathrm{GA})}_{s,\mathrm{c.m.}}(Q,E)$ in order to work out the non-GA contributions and to study their behavior as a function of both Q and liquid density and concentration. Each topic will be dealt with in a separate subsection.

A. Understanding the crossover between diffusional and free-particle regimes

As we have observed above, the H_2 c.m. neutron spectra comprised in the momentum transfer range $2.4\,\text{Å}^{-1} < Q < 3.6\,\text{Å}^{-1}$ exhibit a peculiar crossover regime between a diffusional behavior and an almost-free particle recoil. This is evident for both the experimental $S_{s,\mathrm{c.m.}}(Q,E)$ and the simulated $S^{(\mathrm{GA})}_{s,\mathrm{c.m.}}(Q,E)$ obtained by means of the GA. Obviously, as we will see in the last part of this section, differences between $S_{s,\mathrm{c.m.}}(Q,E)$ and $S^{(\mathrm{GA})}_{s,\mathrm{c.m.}}(Q,E)$ indeed exist in both mixture samples, but from a qualitative point of view the agreement is remarkable and can be easily verified by simply inspecting Figs. 2, 3, 6, and 7. This is a crucial point because it allows using the GA as a tool to provide a physical interpretation of the aforementioned crossover regime. The idea is to decompose $S^{(\mathrm{GA})}_{s,\mathrm{c.m.}}(Q,E)$ in single and multiple pseudophonon excitation terms, similarly to what is normally done in the case of incoherent scattering from a monatomic crystalline solid [20]. However, the long-time diffusional behavior typical of the liquid state makes this decomposition slightly more difficult since the modulus of the time-dependent mean square displacement $|\gamma_1(t)|$ [see, e.g., Eq. (A7) in Appendix A] has no upper limit as t grows to infinity, and so the corresponding self-intermediate scattering function $I^{(\mathrm{GA})}_{s,\mathrm{c.m.}}(Q,t)$ cannot be rigorously developed as a power series in Q. Nevertheless, it is possible to solve the problem, for example, by factorizing $I^{(\mathrm{GA})}_{s,\mathrm{c.m.}}(Q,t)$, that is, by splitting $\gamma_1(t)$ into a diffusional part $\gamma_1^{(d)}(t)$ plus a solidlike part $\gamma_1^{(sl)}(t)$. In this way $|\gamma_1^{(sl)}(t)|$ is limited and the power series in Q can be written exactly as

$$I^{(\mathrm{GA})}_{s,\mathrm{c.m.}}(Q,t) = \exp\left[-Q^2\gamma_1^{(d)}(t)\right]\left\{1 - Q^2\gamma_1^{(sl)}(t) + \sum_{n=2}^{\infty}\frac{\left[-Q^2\gamma_1^{(sl)}(t)\right]^n}{n!}\right\}. \quad (5)$$

After applying the Fourier transform to the previous equation and rearranging the sum as explained in Appendix B, one finally obtains

$$S^{(\mathrm{GA})}_{s,\mathrm{c.m.}}(Q,E) = S_s^{(d)}(Q,E) \otimes \left[S_s^{(sl,0)}(Q,E) + S_s^{(sl,1)}(Q,E) + S_s^{(sl,M)}(Q,E)\right], \quad (6)$$

where $\otimes$ stands for the convolution product, $S_s^{(d)}(Q,E)$ is the diffusional term, while $S_s^{(sl,0)}(Q,E)$, $S_s^{(sl,1)}(Q,E)$, and $S_s^{(sl,M)}(Q,E)$ are the solidlike terms and represent the *zero pseudophonon* contribution, the *single pseudophonon* contribution, and the *multipseudophonon* contribution, respectively. Their actual expressions are all given in Appendix B.

Following Eq. (B1), we have split the simulated $f(\omega)$ spectra for the thermodynamic conditions Nos. (vi) and (x) (see Fig. 4) into $f_d(\omega)$ plus $f_{sl}(\omega)$, making use of the following τ_1 values: $\hbar^{-1}\tau_1 = 0.3256$ and $0.5402\,\mathrm{meV}^{-1}$, respectively, for Nos. (vi) and (x). These figures, together with the corresponding D_s values, entailed the respective areas of $f_{sl}(\omega)$ to be $A_{sl} = 0.6977$ and 0.8508, and the respective solidlike c.m. mean square displacements to be $\langle\vec{u}^2\rangle_{sl} = 0.7615$ and $0.5459\,\text{Å}^2$. This choice has been made by exploiting Eq. (B2) in conjunction with the values of the c.m. mean square displacement for polycrystalline solid hydrogen ($\langle\vec{u}^2\rangle_{pc}$) at various temperatures and densities [37], extrapolated to the molecular densities of the present liquid samples by means of a simple Grüneisen model applied to the zero-point values of $\langle\vec{u}^2\rangle_{pc}$. An example of the separation procedure operated on the simulated $f(\omega)$ for sample No. (vi) is plotted in the inset of Fig. 8. Once $f_d(\omega)$ and $f_{sl}(\omega)$ have been obtained, it is straightforward to calculate the distinct GA contributions $S_s^{(d)}(Q,E)$, $S_s^{(sl,0)}(Q,E)$, and $S_s^{(sl,1)}(Q,E)$ or, to be more precise, $S_s^{(d)}(Q,E) \otimes S_s^{(sl,0)}(Q,E)$ and $S_s^{(d)}(Q,E) \otimes S_s^{(sl,1)}(Q,E)$, in the momentum transfer range $2.4\,\text{Å}^{-1} < Q < 3.6\,\text{Å}^{-1}$. These physical quantities have been reported (without including the instrumental resolution) in the main panel of Fig. 8 for sample No. (vi) only, as sample No. (x) yielded very similar spectra. The total (resolution free) $S_{s,\mathrm{c.m.}}^{(\mathrm{GA})}(Q,E)$ has

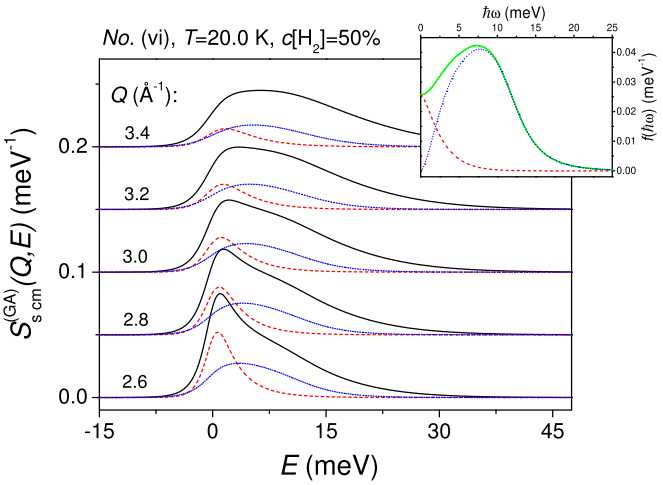

FIG. 8. (Color online) Main panel: GA calculations of the self-part of the para-hydrogen center-of-mass dynamic structure factor $S_{s,\mathrm{c.m.}}^{(\mathrm{GA})}(Q,E)$ in the H_2-D_2 mixture sample No. (vi) (i.e., $c[H_2] = 50.0\%$, see Table II) shown for Q values ranging from 2.6 to $3.4\,\text{Å}^{-1}$ (full black line). The purely diffusional components are also reported (dashed red line) together with the single-pseudophonon terms (dotted blue line). All plots do not include the instrumental resolutions and have been vertically shifted ($0.04\,\mathrm{meV}^{-1}$) for graphic reasons. Inset: separation of the corresponding simulated $f(\omega)$ (green full line) into diffusional (dashed red line) plus solidlike (dotted blue line) terms used for the calculations plotted in the main figure.

been also plotted for comparison. The physical interpretation of this crossover regime from the diffusional behavior to the almost-free particle recoil is now clearer: one observes the purely diffusional term to quickly broaden and lose its intensity as Q grows since the overall peak area is controlled by the solidlike Debye-Waller factor. In addition, the nearby peak, due to the excitation of a single pseudophononic mode combined with molecular diffusion, is also getting broader and decreasing along with Q, but its intensity reduction is less prominent as the solidlike Debye-Waller factor is now contrasted by a Q^2 factor. Finally, the difference between the total spectrum and the sum of the two aforementioned peaks is simply $S_s^{(d)}(Q,E) \otimes S_s^{(sl,M)}(Q,E)$, which although already present at $Q = 2.6\,\text{Å}^{-1}$ (amounting to 34.8% of the total spectrum) becomes the most relevant contribution at larger Q values (reaching 62.1% of the total spectrum at $Q = 3.4\,\text{Å}^{-1}$). Its physical meaning is naturally related to the excitation of two or more pseudophononic modes, always combined with molecular diffusional modes.

B. Extracting two relevant physical quantities

In the previous subsection we have tried to describe, making use of physical models and simulations, the intermediate regime lying between the self-hydrodynamics (roughly dominated by the Fick's laws) and a situation of (almost) free molecular recoil. Now, the target is the opposite: from the extremal regimes we will work out experimental estimates of two physical quantities of key importance for the H_2 c.m. self-dynamics, namely, *self-diffusion coefficient* and *mean kinetic energy*.

An estimate of the H_2 self-diffusion coefficient in the two isotopic liquid mixture samples we are considering here can be obtained by studying their lowest Q-value spectra $S_{s,\mathrm{c.m.}}(Q,E)$, for examples for $1.4\,\text{Å}^{-1} \leqslant Q \leqslant 2.4\,\text{Å}^{-1}$, where the incoherent scattering process probes spatial scales large enough to highlight the diffusional motion of the H_2 centers of mass. However, it is important to stress that IN4C is by no means a spectrometer designed to perform high-precision quasielastic neutron scattering measurements since neither its Q and E ranges, nor the corresponding instrumental resolutions ΔQ and ΔE, are optimized in order to accomplish such a task. For this reason, this study will provide only a tentative estimate of the aforementioned diffusional quantity in a Q range which is normally described as that of *space-dependent self-diffusion* domain [38]. In order to circumvent all the difficulties entailed by such a space-dependent diffusional regime (where a complete theory for quantum and semiquantum fluids does not exist yet), we have focused on one simple spectral feature, namely, the full width at half maximum (FWHM). So, the selected $S_{s,\mathrm{c.m.}}(Q,E)$ spectra have been fitted by a heuristic multi-Voigtian model (up to three independent Voigt function peaks) which has been analytically deconvoluted for the effect of the instrumental energy resolution. Subsequently, the resolution-free fitted data have been corrected for the detailed balance effects by multiplying each spectrum by $\exp[-E/(2k_BT)]$, so to obtain an approximately symmetric peak profile. At this stage, FWHM values have been determined through an interpolation

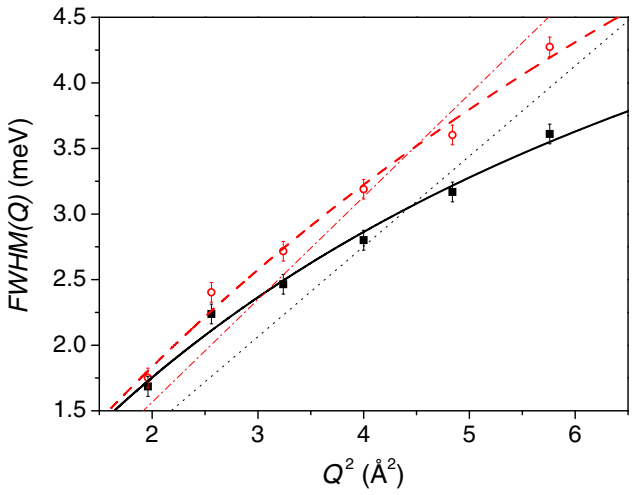

FIG. 9. (Color online) Experimental estimates of full width at half maximum of the para-hydrogen center-of-mass dynamic structure factor $S_{s,\mathrm{c.m.}}(Q,E)$ in the H_2-D_2 mixture samples Nos. (4) (full black squares with error bars) and (5) (empty red circles with error bars). Only the lowest momentum transfer values (i.e., $1.4\ \text{Å}^{-1} \leqslant Q \leqslant 2.4\ \text{Å}^{-1}$) have been considered for such an analysis. Full black and dashed red lines represent data best fits obtained assuming a jump-diffusion model for samples Nos. (4) and (5), respectively. Dotted black and dotted-dashed red lines stand for analogous data best fits, but using a continuous diffusion model.

procedure yielding the estimates reported in Fig. 9 for samples Nos. (4) and (5) in the $1.4\ \text{Å}^{-1} \leqslant Q \leqslant 2.4\ \text{Å}^{-1}$ range. These results were first analyzed via a standard continuous diffusion model: $\mathrm{FWHM}(Q) = 2\hbar D_s Q^2$, which is generally appropriate for simple liquids in the hydrodynamic regime. However, this model, as shown in the mentioned figure, did not provide a good experimental data description since reduced χ^2 turned out to be 19.5 and 11.8 for samples Nos. (4) and (5), respectively. On the other hand, the fitted values of D_s, namely, $0.52(3)\ \text{Å}^2\ \text{ps}^{-1}$ for sample No. (4) and $0.59(2)\ \text{Å}^2\ \text{ps}^{-1}$ for sample No. (5), compared fairly well with the corresponding simulation results reported in Table II [i.e., $0.439(1)\ \text{Å}^2\ \text{ps}^{-1}$ and $0.535(1)\ \text{Å}^2\ \text{ps}^{-1}$], especially if one keeps in mind our preliminary considerations about IN4C. Motivated by this partially successful result, we applied to our FWHM data a slightly more advanced fitting function, i.e., the well-known jump-diffusion model [1]: $\mathrm{FWHM}(Q) = 2\hbar D_s Q^2/(1 + l_0^2 Q^2)$, with l_0 being the mean jump length. Looking again at Fig. 9 one can see that this approach is much more adequate to describe our data (reduced χ^2 fell to 1.27 and 1.91), but D_s came out almost identical for the two cases: $0.86(6)\ \text{Å}^2\ \text{ps}^{-1}$ and $0.81(5)\ \text{Å}^2\ \text{ps}^{-1}$, with all the differences between the two data sets now concentrated in the l_0 estimates: 0.38(3) and 0.28(3) Å for samples Nos. (4) and No. (5), respectively. The large discrepancy between the new D_s fitted values on one side and the simulation results on the other, together with the experimental estimates by O'Reilly and Peterson [39] [namely, $D_s = 0.6(1)\ \text{Å}^2\ \text{ps}^{-1}$ for $c[\mathrm{H_2}] = 50\%$ and $T = 20$ K], actually suggests a certain skepticism about the capability of the jump-diffusion model to properly describe our experimental data despite the good values of the reduced χ^2 obtained. However, in partial contradiction with this remark, we have also to mention the existence of two recent high-resolution neutron spectroscopic studies on liquid [40] and solid [41] molecular hydrogen. In particular, the former includes a measurement on bulk liquid n-H_2 at $T = 15$ K in the $0.45\ \text{Å}^{-1} \leqslant Q \leqslant 1.73\ \text{Å}^{-1}$ range, which clearly detects the presence on a mild jump-diffusion behavior [i.e., $D_s = 0.43(1)\ \text{Å}^2\ \text{ps}^{-1}$ and $l_0 = 0.29(3)$ Å]. Thus, the problem seems indeed quite puzzling, and we think that only accurate quasielastic neutron scattering measurements in a large Q range would be able to completely clarify the diffusional behavior of H_2 molecules in liquid isotopic mixtures. However, given the present scenario, three different hypotheses can be proposed: (1) the observed behavior of the FWHM's as a function of Q is indeed the mark of a jump-diffusion mechanism; (2) it is an artifact caused by the presence of a small inelastic background [1] (which, in turn, is entailed by the relatively large Q values analyzed); (3) it is still an artifact, but actually due to the intrinsic inaccuracies of the deconvolution procedure applied to our neutron scattering spectra. Since the first hypothesis is clearly incompatible with the GA (because jump diffusion implies a nonlinear dependence of FWHM on Q^2), while the second is well described in this framework (as we have seen in Sec. V A), we can shed some light on this intriguing issue by applying the same analytic procedure that we have just described to our GA simulated spectra reported in Figs. 6 and 7. In addition, in order to take into account the third hypothesis too, we decided to work on resolution-free simulated data so to completely circumvent the possible deconvolution problems. It turned out that simulated-data FWHM's were very well described by the continuous diffusion model $\mathrm{FWHM}(Q) = 2\hbar D_s Q^2$, with D_s equal to $0.543(1)\ \text{Å}^2\ \text{ps}^{-1}$ for sample No. (vi) and $0.457(2)\ \text{Å}^2\ \text{ps}^{-1}$ for sample No. (x). These figures, although slightly overestimated with respect to the values reported in Table II, compare quite favorably with them, showing that the possible presence of an inelastic background is not responsible for large errors, and, moreover, cannot induce the observed nonlinear behavior in the experimental-data FWHM's. Thus, while the second hypothesis is ruled out, one still does not know whether the aforementioned nonlinear behavior has a physical non-GA origin or is associated with the deconvolution procedure.

As for the c.m. mean kinetic energy, it is generally possible to estimate its value from the second moment [11] of $S_{s,\mathrm{c.m.}}(Q,E)$ at any constant Q value. However, this procedure becomes practically viable only when Q grows to such an extent that the impulsive regime [20] is approached. This happens because under these conditions the peak shape tends to a simple Gaussian functional form (provided that the single-particle momentum distribution is indeed a Gaussian) and, in addition, the peak width gets progressively wider (so that the energy resolution turns out to be almost insignificant). This phenomenon is currently exploited by the so-called *deep inelastic neutron scattering* (also known as *neutron Compton scattering*) which has been successfully applied to various systems [42], including molecular hydrogen in condensed phases [43], providing accurate estimates of the H_2

center-of-mass mean kinetic energy. A simple method to verify the inception of the impulsive regime is the application of the so-called West y scaling [44], where $S_{s,\mathrm{c.m.}}(Q,E)$ is replaced by the response function $F(y,Q)$ according to the following scaling equations:

$$y = \frac{2m_{\mathrm{H}}}{\hbar^2 Q}\left(E - \frac{\hbar^2 Q^2}{4m_{\mathrm{H}}}\right); \quad F(y,Q) = \frac{\hbar^2 Q}{2m_{\mathrm{H}}} S_{s,\mathrm{c.m.}}(Q,E). \tag{7}$$

Now, it is possible to prove [44] that in most physical cases the explicit dependence of $F(y,Q)$ on Q gradually vanishes and an asymptotic regime [i.e., $J(y)$] is progressively approached. In the case of molecular liquid hydrogen, this surely happens for $Q > 4.9\,\text{Å}^{-1}$ [45], but in our case we see in Fig. 10 that for $3.6\,\text{Å}^{-1} \leqslant Q \leqslant 4.6\,\text{Å}^{-1}$ the experimental West response function $F_e(y,Q)$ changes very weakly as a function of Q. Nevertheless, the asymptotic regime is clearly not yet attained as shown by the asymmetric peak shapes and by the fact that the peak maximum does not coincide with $y = 0$. This is the typical mark of the persistence of the so-called *final state effects* [44] which are caused by the influence of the intermolecular potential on the recoil of the H_2 molecule hit by the scattered neutron. By fitting the $F_e(y,Q)$ data sets for both samples Nos. (4) and (5) through a heuristic multi-Gaussian model (i.e., four independent Gaussian peaks), it is possible to extract the various second moment $\langle y^2\rangle$ estimates, which, once corrected for their average instrumental resolutions $\overline{\Delta E}$, are independent of Q and are related to the c.m. mean kinetic energy through the relationship [44]

$$\langle y^2\rangle = \int_{-\infty}^{\infty} y^2 F_e(y,Q)dy - \frac{1}{8\ln(2)}\left(\frac{2m_{\mathrm{H}}}{\hbar^2 Q}\overline{\Delta E}\right)^2 = \frac{4m_{\mathrm{H}}}{3\hbar^2}\langle E_k\rangle. \tag{8}$$

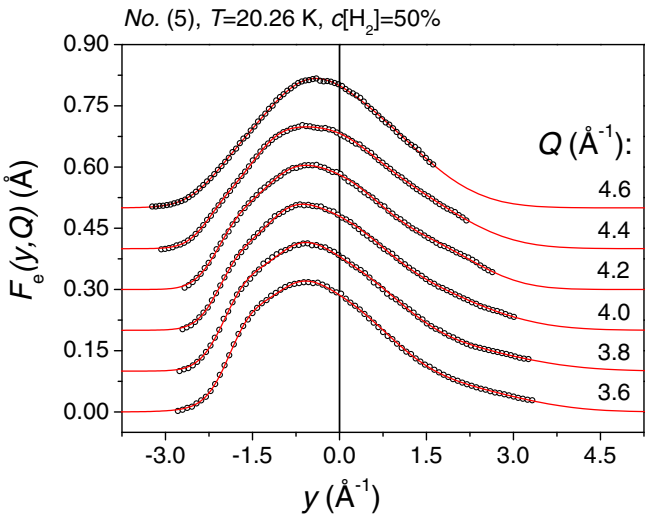

FIG. 10. (Color online) Experimental estimates of the West-scaling response function $F_e(y,Q)$ in the H_2-D_2 mixture sample No. (5) (empty black circles), and their best multi-Gaussian fits (full red lines). Only the highest momentum transfer values (i.e., $3.6\,\text{Å}^{-1} \leqslant Q \leqslant 4.6\,\text{Å}^{-1}$) have been considered for such an analysis. Spectra, derived from data plotted in Fig. 3, have been vertically shifted (0.1 Å) for graphic reasons.

It turned out that the values obtained were $\langle E_k\rangle = (61 \pm 3)$ K and (58 ± 3) K, respectively, for samples Nos. (4) and (5). In Fig. 10, we have reported the y-scaled experimental data for sample No. (5) for $3.6\,\text{Å}^{-1} \leqslant Q \leqslant 4.6\,\text{Å}^{-1}$ together with their best multi-Gaussian fits. We can easily observe that despite the good quality of the fit, the reconstruction of the peak profile is only hypothetical since experimental data do not cover all the y range needed for a full evaluation of $\langle y^2\rangle$. In particular, the peak tails, which contribute in a substantial way to the $\langle y^2\rangle$ evaluation, were not completely probed by the present neutron measurements and had to be extrapolated by the fitting procedure. For this reason, we think that the moderate agreement between simulated values, namely, $\langle E_k\rangle = (71.1 \pm 0.7)$ K and (68.1 ± 0.7) K, respectively, for samples Nos. (4) and (5) as from Table II, and experimental ones is not to be regarded as a serious problem.

C. Studying the non-Gaussian components

The non-Gaussian contributions to the c.m. self-dynamics structure factor, dubbed $\delta_{n\mathrm{GA}}S_{s,\mathrm{c.m.}}(Q,E)$, can be easily obtained from

$$\delta_{n\mathrm{GA}}S_{s,\mathrm{c.m.}}(Q,E) = S_{s,\mathrm{c.m.}}(Q,E) - S^{(\mathrm{GA})}_{s,\mathrm{c.m.}}(Q,E), \tag{9}$$

where both the experimental $S_{s,\mathrm{c.m.}}(Q,E)$ and the CMD-simulated $S^{(\mathrm{GA})}_{s,\mathrm{c.m.}}(Q,E)$ are meant to include the instrumental energy resolution $\Delta E(E)$, which, as seen in Sec. III, is not constant, but slowly varying with E. It is reasonable to describe the resolution effect via a convolution with a Gaussian function $G_{\sigma(E)}(E)$, where the parametric dependence on $\sigma(E)$ is given by $\sigma(E) \approx 0.4246609\Delta E(E + E_{0-1})$. Results for the non-Gaussian contributions in samples Nos. (4) and (5) are reported in Figs. 11 and 12, respectively, for some selected Q values ranging from 1.4 to 4.2 Å^{-1}. We immediately see that the two $\delta_{n\mathrm{GA}}S_{s,\mathrm{c.m.}}(Q,E)$ spectral sets look very similar

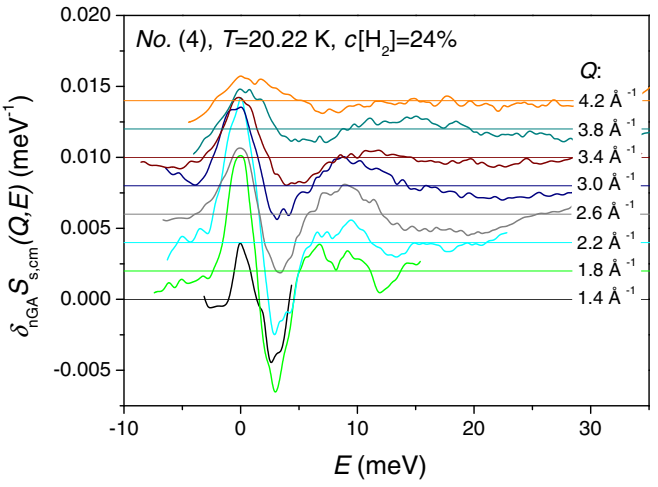

FIG. 11. (Color online) Non-Gaussian components of the self-part of the para-hydrogen center-of-mass dynamic structure factor $\delta_{n\mathrm{GA}}S_{s,\mathrm{c.m.}}(Q,E)$, in the H_2-D_2 mixture sample No. (4) (i.e. $c[H_2] = 24\%$, see Table I) shown for some selected Q values ranging from 1.4 Å^{-1} (black full line, bottom) to 4.2 Å^{-1} (full orange line, top). Spectra have been vertically shifted (0.002 meV^{-1}) for graphic reasons.

to each other, as far the overall shape is concerned, while, dealing with the intensity, sample No. (4) ($c[H_2] = 24\%$) exhibits non-Gaussian components which are substantially more intense than those belonging to sample No. (5) ($c[H_2] = 50\%$). Focusing on a single data set, one can observe the Q variation of these spectral components even though they are slightly noisy: most of the intensity is localized in the (−5–5) meV energy range, becoming first positive and then negative, followed by other weaker oscillations at larger E values. Spectra tend to grow from $Q = 1.4\,\text{Å}^{-1}$ to a maximum around $2.2\,\text{Å}^{-1}$, then they quickly lose intensity (at about $2.6\,\text{Å}^{-1}$), and finally decrease very slowly up to $Q = 4.2\,\text{Å}^{-1}$.

Following Refs. [46] and [47], it is possible to write the non-Gaussian contributions as

$$\begin{aligned}\delta_{n\text{GA}} S_{s,\text{c.m.}}(Q,E) &= \int_{-\infty}^{\infty} dE' G_{\sigma(E)}(E-E') \frac{Q^4}{4\pi\hbar} \\ &\times \int_{-\infty}^{\infty} dt\, e^{-iE'\hbar^{-1}t - Q^2\gamma_1(t)} \gamma_1^2(t)\alpha_2(t) \\ &= \frac{Q^4}{4\pi\hbar} \int_{-\infty}^{\infty} dt \exp\left[-iE\hbar^{-1}t - \frac{\sigma^2(E)t^2}{2\hbar^2}\right] \\ &\times e^{-Q^2\gamma_1(t)} \gamma_1^2(t)\alpha_2(t), \end{aligned} \tag{10}$$

where $\alpha_2(t)$ is the first correction term to the GA [46,47], which is actually unknown. So, since $G_{\sigma(E)}(E)$ is experimentally known and $\gamma_1(t)$ can be derived from the quantum simulations, the spectra reported in Figs. 11 and 12 provide useful information on $\alpha_2(t)$ for samples Nos. (4) and (5). Since $\alpha_2(t)$ is independent of Q there is no need to work on all the spectra contained in each data set. It is enough to select a Q value connected with the most intense $\delta_{n\text{GA}} S_{s,\text{c.m.}}(Q,E)$ components (i.e., $2.2\,\text{Å}^{-1}$), to evaluate the corresponding $\exp[-Q^2\gamma_1(t)]Q^4\gamma_1^2(t)/2$ data, and, finally, to approximately

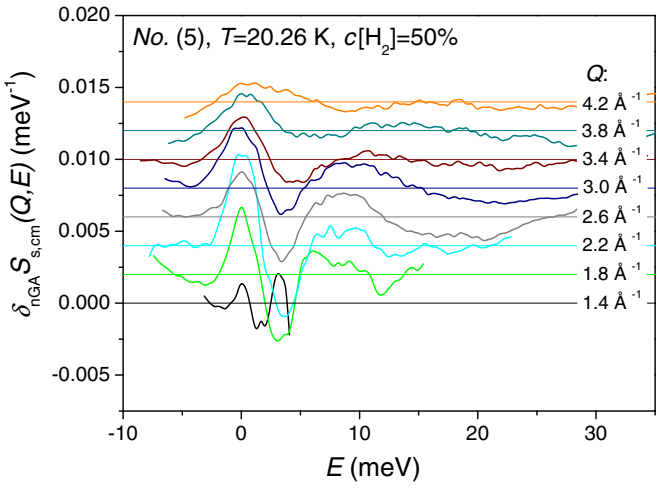

FIG. 12. (Color online) Non-Gaussian components of the self-part of the para-hydrogen center-of-mass dynamic structure factor $\delta_{n\text{GA}} S_{s,\text{c.m.}}(Q,E)$, in the H_2-D_2 mixture sample No. (5) (i.e., $c[H_2] = 50\%$, see Table I) shown for some selected Q values ranging from $1.4\,\text{Å}^{-1}$ (black full line, bottom) to $4.2\,\text{Å}^{-1}$ (full orange line, top). Spectra have been vertically shifted ($0.002\,\text{meV}^{-1}$) for graphic reasons.

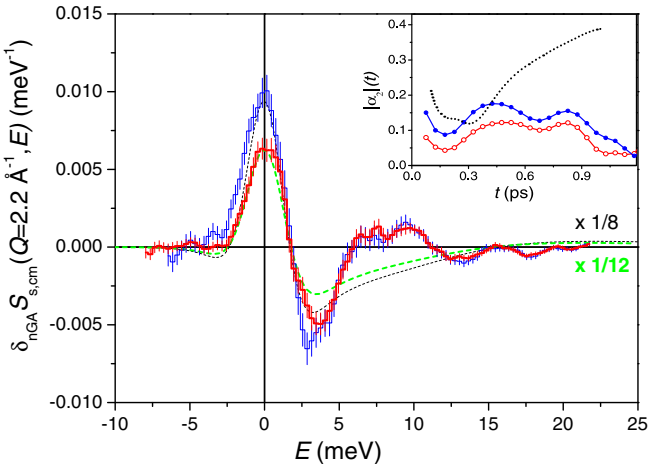

FIG. 13. (Color online) Main panel: non-Gaussian components of the self-part of the para-hydrogen center-of-mass dynamic structure factor $\delta_{n\text{GA}} S_{s,\text{c.m.}}(Q = 2.2\,\text{Å}^{-1}, E)$, in the H_2-D_2 mixture samples No. (4) (thin blue histogram) and (5) (thick red histogram), together with the corresponding Fourier transforms of $\exp[-\sigma^2(0)t^2/(2\hbar^2) - Q^2\gamma_1(t)]Q^4\gamma_1^2(t)/2$, plotted as thin black dashes and thick green dashes, respectively. The latter two (simulated) spectra have been scaled for graphic reasons. Inset: modulus (symbols plus line) of the first non-Gaussian coefficient $\alpha_2(t)$ for samples Nos. (4) (full blue circles) and (5) (empty red circles). These two full lines are only a guide for the eye, while the dotted black line represents $|\alpha_2(t)|$ for pure para-hydrogen elaborated from data in Ref. [7].

extract $\alpha_2(t)$ through a Fourier antitransform:

$$\alpha_2(t) \approx \frac{\int_{-\infty}^{\infty} dE \exp\left(i\frac{Et}{\hbar}\right)\delta_{n\text{GA}} S_{s,\text{c.m.}}(Q,E)}{\frac{1}{2}\exp\left[-\frac{\sigma^2(E=0)t^2}{2\hbar^2} - Q^2\gamma_1(t)\right]Q^4\gamma_1^2(t)}, \tag{11}$$

making use of a fixed energy resolution [namely, its value at the $j = 0 \to j' = 1$ rotational line of H_2, $\Delta E(E_{0-1})$] since this quantity does not change too rapidly in the energy transfer range where most of the signal intensity is located. However, due to the fact that for $Q = 2.2\,\text{Å}^{-1}$ one has $\Delta E(E_{0-1}) = 2.54$ meV, then time values larger than $t_M = 0.815$ ps are gradually less and less meaningful: unfortunately, the energy resolving power of the spectrometer does not allow inferring information on the long-time behavior of $\alpha_2(t)$, but only on its onset. It is worth noting that in Eq. (11) one always deals with complex functions, so $\alpha_2(t)$ comes out with two components: $\text{Re}[\alpha_2(t)]$ and $\text{Im}[\alpha_2(t)]$. In the main panel of Fig. 13, we have plotted $\delta_{n\text{GA}} S_{s,\text{c.m.}}(Q = 2.2\text{Å}^{-1}, E)$ together with the Fourier transform of $\exp[-\sigma^2(0)t^2/(2\hbar^2) - Q^2\gamma_1(t)]Q^4\gamma_1^2(t)/2$, still for samples Nos. (4) and (5); while in the inset of Fig. 13, we have reported the modulus of $\alpha_2(t)$, $|\alpha_2(t)|$ for both the aforementioned samples. In addition, $|\alpha_2(t)|$ for pure liquid para-hydrogen at $T = 15.7$ K and $n = 22.53\,\text{nm}^{-3}$, derived from data in Ref. [7], has been also plotted. The comparison of the latter sample with the two mixtures makes sense, although its temperature was rather lower than that of the mixtures, because the H_2 diffusion coefficient $D_s = 0.495\,\text{Å}^2\text{ps}^{-1}$ [7], lies between the two mixture values [see simulations Nos. (vi) and (x) in Table II]. One can see that while the behavior of $|\alpha_2(t)|$ for the two mixtures is similar, even though the

non-GA correction is clearly more intense in the higher density (and lower H_2 concentration) case, the same quantity in pure liquid para-hydrogen looks rather different, starting close to the corresponding curve for sample No. (4), but then getting more intense and growing for a longer time. The physical interpretation of these findings is not straightforward at the moment, but it is not unrealistic to think that it is related to the intensity of the cage effects on H_2 molecules caused by the presence of heavier D_2 molecules, which are obviously absent in the pure H_2 sample. As for possible comparisons between the non-Gaussian self-dynamics in H_2 (and H_2-D_2 mixtures) on one side, and that in other systems on the other, we will limit ourselves to a few general comments: We have shown in a very recent paper [47] that what might exhibit a strong mathematical analogy reveals, on the other hand, deep physical differences which practically prevent such comparisons. As a matter of fact, the non-Gaussian components of the intermediate self-scattering function $I_s(Q,t)$ can be classed in three broad groups completely disconnected from one another: (i) strongly quantum fluid (e.g., superfluid ^{4}He) where the short-time behavior of non-Gaussian components of the $I_s(Q,t)$ is dominated by t^4; (ii) semiquantum fluids (e.g., liquid H_2, D_2 and their mixtures) where the short-time behavior of these physical quantities is dominated by t^5; (iii) classical liquids, where this short-time behavior is dominated by t^8. It is evident from this fact that the mechanisms which control the origin of the non-Gaussian self-dynamics have to be completely different in the three aforementioned groups.

However, despite these profound physical differences, we think that a possible analogy between semiquantum liquids on one side, and polymers and other soft-matter systems on the other, could be established (as far as the breakdown of the GA is concerned) in the light of the isomorphism (see Sec. IV) between a single quantum delocalized particle and a fictitious cyclic chain including a large number of classical particles (the so-called "beads"). We have seen that this is the core of the PIMC simulation procedure as well as various dynamic techniques derived from it (e.g,. CMD and RPMD). By taking into account the phenomenological description of the classical non-Gaussian self-dynamics provided by Tsang [48], we manage to draw an interesting picture of this fascinating physical phenomenon. At the end of his paper, Tsang states that the function $I_s(Q,t)$ deviates from a Gaussian function of Q at time t because it can be expressed as a sum of Gaussian functions $I_s(u_1|Q,t)$ weighted by the probability distribution $p(u_1)$. We remind that, according to Tsang, if "0" is the tagged particle, then u_1 is the velocity component for its nearest neighbor particle "1" projected onto the position vector $(\vec{r}_0 - \vec{r}_1)$. This deviation from a Gaussian functional shape, generally speaking, comes from the non-Gaussian nature of the fluctuating random force $\vec{A}_{10}(t)$, acting on the tagged particle "0" and originated from its nearest neighbor particle "1." In the case of a classical system, the non-Gaussian interparticle forces can be associated with the strong and long-lasting spatial correlations between a molecule and its surroundings like, for example, in the well-known "caging effect." In a semiquantum system, on the other hand, monomers (i.e., the fictitious "beads") isomorphically represent a single quantum particle coherently delocalized over a certain volume. Each bead interacts with its two nearest neighbors (in the same chain polymer) via the so-called "quantum harmonic potential": $U(x) = m_H P \hbar^{-2} k_B^2 T^2 x^2$ (x being the distance between two adjacent beads), but also with the all the corresponding beads belonging to the other fictitious cyclic chains through the standard intermolecular potential $P^{-1}V(r)$ [49]. Thus, both quantum coherence and intermolecular interactions have to be considered in order to give rise to an analogous pseudocaging effect. Needless to say, this comparison between soft matter systems and semiquantum fluids has been just sketched and surely deserves further attention.

VI. CONCLUSIONS

In conclusion, in this study we have measured the incoherent inelastic neutron spectrum of liquid para-hydrogen mixed with normal deuterium ($T = 20$ K) at two different H_2 molar concentrations (namely, 24% and 50%) using the time-of-flight neutron spectrometer IN4C [14]. The recorded double-differential cross sections have provided direct experimental access to the self-part of the dynamic structure factor for the H_2 centers of mass in the two mixture samples under observation. Experimental data were corrected for the typical experimental effects, and then analyzed in the framework of the generalized Young-Koppel model [10,24] to remove the contributions from intramolecular (i.e., rotovibrational) dynamics. In this way, one ended up with a complete mapping of the H_2 center-of-mass self-dynamics structure factor in the momentum transfer interval (1.4–4.6) Å^{-1} and in the energy transfer interval (−10–40) meV, with an average energy resolution of about 2–4 meV. The low-momentum transfer part of the processed data was studied in order to extract information of the H_2 diffusional motion in the liquid mixtures, despite the fact that IN4C is not the most suitable instrument for quasielastic neutron scattering studies. However, after a careful deconvolution procedure, we managed to work out the spectral features related to the H_2 diffusion. They turned out to be in a reasonable agreement with the self-diffusion coefficients simulated by quantum calculations or reported in the literature [39], although our experimental estimates of the self-diffusion coefficients exhibit a peculiar variation as a function of the momentum transfer which seems compatible with a jump-diffusion mechanism, similarly to what has been observed in bulk liquid n-H_2 at $T = 15$ K [40]. However, at the present stage, no final conclusion on this subject can be drawn. In addition, from the high-momentum transfer part of the processed data the mean kinetic energy of the H_2 centers of mass was estimated making use of the West y scaling [44] for the molecular translational dynamics in the liquid, and then compared with accurate quantum calculations. The agreement was found to be only fairly good because, for intrinsic kinematic reasons, the y-transformed experimental data were not complete and had to be extrapolated via a heuristic fitting procedure. The aforementioned quantum calculations, the so-called *centroid molecular dynamics* [3] to be more precise, also provided estimates of the velocity autocorrelation function for the H_2 centers of mass. These estimates, in conjunction with the well-known Gaussian approximation [11], were used to simulate the H_2 center-of-mass self-dynamics structure factor

in the same range as the experimental one. This simulation was particularly useful for the intermediate momentum transfer spectra where the complex crossover regime from diffusion to almost-free recoil was understood in a clear and sound physical framework. However, the agreement between measured and calculated spectra was globally good, but some discrepancies (particularly relevant in the momentum transfer range (1.8–3.2) Å^{-1}) proved the unquestionable breakdown of the Gaussian approximation in these semiquantum systems at a level slightly lower than that already observed in pure liquid para-hydrogen [7,8], but clearly depending on the molecular density of the sample. Thus, the present results appear of great interest, confirming our old preliminary and incomplete measurements [13], and suggesting the need to apply some care in the use of the Gaussian approximation with H_2-containing semiquantum fluids. In addition, it is also suggested that detailed quasielastic neutron scattering studies on the H_2 motion in the hydrogen-deuterium liquid mixtures in order to clarify the nature of the diffusion mechanism are greatly needed.

ACKNOWLEDGMENT

The Scientific Membership Agreement (Protocol AMMCNT - CNR No. 0015971) between Consiglio Nazionale delle Ricerche (Italy) and Institut Laue-Langevin (ILL, France) and the skillful technical assistance of ILL staff (especially on cryogenics by Mr. Simon Baudoin) are gratefully acknowledged.

APPENDIX A

The Egelstaff and Schofield (ES) model for the self-dynamics structure factor $S_s^{(\mathrm{ES})}(Q,E)$ of a monatomic fluid has been originally devised [50] in a classical framework. Despite the existence of an analytical expression for $S_s^{(\mathrm{ES})}(Q,E)$ provided by this model, it is much easier and physically more meaningful to report its time Fourier transform, i.e., the self-intermediate scattering function $I_s^{(\mathrm{ES})}(Q,t)$, which reads as

$$I_s^{(\mathrm{ES})}(Q,t) = \exp\left[-Q^2 D_s\left(\sqrt{t^2+\tau_0^2}-\tau_0\right)\right], \tag{A1}$$

where $\tau_0 = D_s M/(k_B T)$ with M being the atomic mass. So, in the long-time limit ($t \to \pm\infty$), where $\sqrt{t^2+\tau_0^2}-\tau_0 \approx |t|$, the ES model tends to the standard diffusional behavior [20]

$$I_s^{(\mathrm{ES})}(Q,t) \approx \exp(-Q^2 D_s |t|). \tag{A2}$$

On the contrary, for short values of time ($t \to 0^{\pm}$), where $\sqrt{t^2+\tau_0^2}-\tau_0 \approx t^2/(2\tau_0)$, the ES model converges to the classical (i.e., without recoil) free gas behavior [20]

$$I_s^{(\mathrm{ES})}(Q,t) \approx \exp\left(-Q^2 \frac{k_B T}{2M} t^2\right). \tag{A3}$$

The ES model can be surely interpreted in the framework of the classical version of the GA [20]

$$I_s(Q,t) = \exp\left\{-\frac{Q^2 k_B T}{M}\int_0^\infty \frac{p(\omega)}{\omega^2}[1-\cos(\omega t)]d\omega\right\}, \tag{A4}$$

so to give, after a double differentiation and a cosine transform inversion, a simple expression for the power spectrum of the classical VACF, $p(\omega)$:

$$\begin{aligned} &\frac{k_B T}{M}\int_0^\infty \frac{p_{\mathrm{ES}}(\omega)}{\omega^2}[1-\cos(\omega t)]d\omega = D_s\left(\sqrt{t^2+\tau_0^2}-\tau_0\right); \\ &\int_0^\infty p_{\mathrm{ES}}(\omega)\cos(\omega t)d\omega = \tau_0^3\left(t^2+\tau_0^2\right)^{-3/2}; \\ &p_{\mathrm{ES}}(\omega) = \frac{2\tau_0}{\pi}\tau_0\omega K_1(\tau_0\omega), \end{aligned} \tag{A5}$$

with $K_1(x)$ being a modified Bessel function of the second kind (first order). In this way, $p_{\mathrm{ES}}(0) = 2MD_s/(\pi k_B T)$ as expected. Various attempts have been accomplished in order to extend the ES model to quantum fluids, all led by the idea to keep a simple three-parameter (T, M, and D_s) expression. The most common correction scheme (ES*) yields the following analytical expression for the quantum $I_s(Q,t)$ [25]:

$$I_s^{(\mathrm{ES}^*)}(Q,t) = \exp\left\{-Q^2 D_s\left[\sqrt{t\left(t-i\frac{\hbar}{k_B T}\right)+\tau_0'^2}-\tau_0'\right]\right\}, \tag{A6}$$

where $\tau_0' = \sqrt{\tau_0^2+\hbar^2/(2k_B T)^2}$. Here, we report a different approach to devise a simple quantum Egelstaff and Schofield (QES) model. The starting point is the correct quantum GA [11]:

$$\begin{aligned} I_s(Q,t) &= \exp[-Q^2\gamma_1(t)] \\ &= \exp\left(-\frac{\hbar Q^2}{2M}\int_0^\infty \frac{f(\omega)}{\omega}\left\{\coth\left(\frac{\hbar\omega}{2k_B T}\right)\right.\right. \\ &\quad \left.\left.\times[1-\cos(\omega t)] - i\sin(\omega t)\right\}d\omega\right), \end{aligned} \tag{A7}$$

where $\gamma_1(t)$ is one third of the time-dependent c.m. mean square displacement, and $f(\omega)$ is defined in Eq. (2). However, it is simpler to make use of a fully equivalent formalism: the GA for the symmetrized intermediate scattering function $\tilde{I}(Q,t)$, which is a real function and reads as [11]

$$\begin{aligned} \tilde{I}_s(Q,t) &= I\left(Q,t+i\frac{\hbar}{2k_B T}\right) = \exp[-Q^2\tilde{\gamma}_1(t)] \\ &= \exp\left\{-\frac{\hbar Q^2}{2M}\int_0^\infty \frac{f(\omega)}{\omega}\coth\left(\frac{\hbar\omega}{2k_B T}\right)\right. \\ &\quad \left.\times\left[1-\cos(\omega t)\mathrm{sech}\left(\frac{\hbar\omega}{2k_B T}\right)\right]d\omega\right\}. \end{aligned} \tag{A8}$$

We can see that in the classical limit ($\hbar \to 0$), Eq. (A8) coincides with Eq. (A4) provided that $f(\omega) = p_{\mathrm{ES}}(\omega)$. Thus, our version of the QES method is simply based on Eq. (A8) itself together with the *ansatz*

$$f_{\mathrm{QES}}(\omega) = \frac{2\tau_0}{\pi}\tau_0\omega K_1(\tau_0\omega). \tag{A9}$$

Putting all the parts together, one finally writes

$$S_s^{(\mathrm{QES})}(Q,E) = \frac{e^{E/(2k_BT)}}{2\pi\hbar}\int_{-\infty}^{\infty} e^{-i\hbar^{-1}Et} \times \exp\left\{-\frac{\hbar\tau_0^2Q^2}{\pi M}\int_0^{\infty} K_1(\tau_0\omega)\coth\left(\frac{\hbar\omega}{2k_BT}\right) \times\left[1-\cos(\omega t)\,\mathrm{sech}\left(\frac{\hbar\omega}{2k_BT}\right)\right]d\omega\right\}dt, \quad \text{(A10)}$$

where the link between $\tilde{S}_s(Q,E)$ and $S_s(Q,E)$ has been also used. The QES model is correctly normalized (zeroth moment), exhibits an exact recoil (first moment), complies with the detailed balance, and shows a rigorous long-time diffusional behavior. However, as far as the second moment (and the following ones) are concerned, results are only approximate. For example, the single-particle mean kinetic energy $\langle E_k\rangle$ comes out to be given by

$$\langle E_k\rangle = \frac{3\hbar\tau_0^2}{2\pi}\int_0^{\infty}\omega^2 K_1(\tau_0\omega)\coth\left(\frac{\hbar\omega}{2k_BT}\right)d\omega, \quad \text{(A11)}$$

which in general is not exact, even though its classical limit ($\hbar\to 0$) is indeed correct: $\langle E_k\rangle = 3k_BT/2$. As an example, we report the results from Eq. (A11) in conjunction with the diffusion coefficients of the simulated sample (vi) (see Table II), namely, $D_{s,\mathrm{H_2}} = 0.535\,\text{Å}^2\,\mathrm{ps}^{-1}$ and $D_{s,\mathrm{D_2}} = 0.499\,\text{Å}^2\,\mathrm{ps}^{-1}$. CMD provides the following results for the mean kinetic energy extracted from the VACF spectra: $\langle E_k\rangle^f_{\mathrm{H_2}} = 67.44$ K and $\langle E_k\rangle^f_{\mathrm{D_2}} = 52.09$ K, while the QES model gives $\langle E_k\rangle_{\mathrm{H_2}} = 117.40$ K and $\langle E_k\rangle_{\mathrm{D_2}} = 68.70$ K, which are overestimated for both isotopes. The latter pair of kinetic energy values can be compared with the corresponding figures obtained in the framework of the quantum corrected ES* model devised in Ref. [25] and reported in Eq. (A6):

$$\langle E_k\rangle = \frac{3}{2}k_BT\left(1+\frac{\hbar^2}{4M^2D_s^2}\right), \quad \text{(A12)}$$

namely, $\langle E_k\rangle_{\mathrm{H_2}} = 290.07$ K and $\langle E_k\rangle_{\mathrm{D_2}} = 104.91$ K, which are even more largely overestimated. The reason of the worse performance by the model in Eq. (A6) with respect to the QES one is easily explained if one considers the functional form of $f(\omega)$ in the two cases. As a matter of fact, it is possible to show that Eq. (A6) is fully equivalent to the quantum GA in Eq. (A7) once the following VACF spectrum is assumed:

$$f_{\mathrm{ES}^*}(\omega) = \frac{4D_sM}{\hbar\pi}\sinh\left(\frac{\hbar\omega}{2k_BT}\right)\tau_0' K_1(\tau_0'\omega). \quad \text{(A13)}$$

In the classical limit ($\hbar\to 0$), $f_{\mathrm{ES}^*}(\omega)$ coincides with $p_{\mathrm{ES}}(\omega)$ [and thence with $f_{\mathrm{QES}}(\omega)$], but if quantum effects become important then $f_{\mathrm{ES}^*}(\omega)$ develops a long tail at large ω values (caused by the hyperbolic sine) which makes $\langle E_k\rangle$ grow in an excessive way. For this reason, we think that our version of the ES model (made suitable for quantum systems) offers better results than the approach reported in Ref. [25].

APPENDIX B

The spectrum $f(\omega)$ of the velocity autocorrelation function [11] in the case of a liquid can be split in two parts: a diffusional component $f_d(\omega)$ plus a solidlike component $f_{sl}(\omega)$, where $f_d(0) = f(0) = 2MD_s/(\pi k_BT)$, and $f_{sl}(0) = 0$. For example, one could assume $f_d(\omega)$ to have a functional form similar to that of $f_{\mathrm{QES}}(\omega)$ in Eq. (A9), namely,

$$\begin{aligned} f_d(\omega) &= f(0)\omega\tau_1 K_1(\omega\tau_1);\\ f_{sl}(\omega) &= f(\omega) - f(0)\omega\tau_1 K_1(\omega\tau_1), \end{aligned} \quad \text{(B1)}$$

with τ_1 being an adjustable parameter to be set in a way that the solidlike behavior of the liquid is reasonably well described. For example, a possible approach for the τ_1 determination could exploit the relationship between the low-ω trend of $f_{sl}(\omega)$ and the effective Debye temperature θ_D of the liquid under investigation (e.g., derived from its sound velocity [51]). Another approach could exploit the value of the solidlike mean square displacement $\langle\vec{u}^2\rangle_{sl}$ [related to $f_{sl}(\omega)$ by a well-known relationship [20]], which should approximately correspond to the same physical quantity in a (hypothetical) polycrystalline solid $\langle\vec{u}^2\rangle_{pc}$, scaled to exhibit similar density and temperature:

$$\langle\vec{u}^2\rangle_{sl} \approx A_{sl}\langle\vec{u}^2\rangle_{pc}, \quad \text{(B2)}$$

where A_{sl} is the total $f_{sl}(\omega)$ normalization and is given by $1 - D_sM/(\tau_1k_BT)$.

Operating this $f(\omega)$ separation in the GA definition, i.e., in Eq. (A7), one can write

$$I_s(Q,t) = \exp\left(-\frac{\hbar Q^2}{2M}\int_0^{\infty}\frac{f_d(\omega)}{\omega}\left\{\coth\left(\frac{\hbar\omega}{2k_BT}\right) \times[1-\cos(\omega t)] - i\sin(\omega t)\right\}d\omega\right) \times\sum_{n=0}^{\infty}\frac{1}{n!}\left(\frac{-\hbar Q^2}{2M}\right)^n\left(\int_0^{\infty}\frac{f_{sl}(\epsilon)}{\epsilon}\left\{\coth\left(\frac{\hbar\epsilon}{2k_BT}\right) \times[1-\cos(\epsilon t)] - i\sin(\epsilon t)\right\}d\epsilon\right)^n \quad \text{(B3)}$$

or, equivalently,

$$I_s(Q,t) = \exp\left[-Q^2\gamma_1^{(d)}(t)\right]\sum_{n=0}^{\infty}\frac{\left[-Q^2\gamma_1^{(sl)}(t)\right]^n}{n!}, \quad \text{(B4)}$$

as implemented in Eq. (5). Alternatively, one can factorize the solidlike Debye-Waller factor too:

$$I_s(Q,t) = \exp\left[-Q^2\gamma_1^{(d)}(t) - 2W^{(sl)}(Q)\right]\sum_{n=0}^{\infty}\frac{\left[Q^2U_1^{(sl)}(t)\right]^n}{n!}, \quad \text{(B5)}$$

where

$$2W^{(sl)}(Q) = \frac{1}{3}\langle \vec{u}^2 \rangle_{sl} Q^2 = \frac{\hbar Q^2}{2M}\int_0^\infty \frac{f_{sl}(\epsilon)}{\epsilon}\coth\left(\frac{\hbar\epsilon}{2k_BT}\right)d\epsilon;$$
$$U_1^{(sl)}(t) = \frac{\hbar}{2M}\int_0^\infty \frac{f_{sl}(\epsilon)}{\epsilon}\left[\coth\left(\frac{\hbar\epsilon}{2k_BT}\right)\cos(\epsilon t) + i\sin(\epsilon t)\right]d\epsilon. \quad \text{(B6)}$$

Performing the Fourier transform of Eq. (B5), one finally writes the so-called multiphonon expansion of the solidlike self-scattering law:

$$S_s(Q,E) = S_s^{(d)}(Q,E) \otimes \sum_{n=0}^{\infty} S_s^{(sl,n)}(Q,E) = S_s^{(d)}(Q,E) \otimes \sum_{n=0}^{\infty} e^{-2W^{(sl)}(Q)} \int_{-\infty}^{\infty} \frac{dt}{2\hbar\pi} e^{-i\hbar^{-1}Et} \frac{\left[Q^2 U_1^{(sl)}(t)\right]^n}{n!}, \quad \text{(B7)}$$

where $\otimes$ stands for the convolution product and $S_s^{(d)}(Q,E)$ is simply given by

$$S_s^{(d)}(Q,E) = \int_{-\infty}^{\infty} \frac{dt}{2\hbar\pi} \exp\left[-i\hbar^{-1}Et - Q^2\gamma_1^{(d)}(t)\right]. \quad \text{(B8)}$$

The first two terms in the sum of Eq. (B7) can be written explicitly as

$$S_s^{(sl,0)}(Q,E) = e^{-2W^{(sl)}(Q)}\delta(E); \quad S_s^{(sl,1)}(Q,E) = \frac{\hbar Q^2}{4M} e^{-2W^{(sl)}(Q)} \frac{f_{sl}(\hbar^{-1}|E|)}{E}\left[\coth\left(\frac{E}{2k_BT}\right) + 1\right], \quad \text{(B9)}$$

while the rest of the sum, dubbed $S_s^{(sl,M)}(Q,E)$, is given by

$$S_s^{(sl,M)}(Q,E) = e^{-2W^{(sl)}(Q)} \sum_{n=2}^{\infty} \int_{-\infty}^{\infty} \frac{dt}{2\hbar\pi} e^{-i\hbar^{-1}Et} \frac{\left[Q^2 U_1^{(sl)}(t)\right]^n}{n!}. \quad \text{(B10)}$$

[1] P. A. Egelstaff, *An Introduction to the Liquid State* (Clarendon Press, Oxford, 1994).

[2] A. F. Andreev and Yu. A. Kosevich, Zh. Eksp. Teor. Fiz. **77**, 2518 (1979) [Sov. Phys.–JETP **50**, 1218 (1979)].

[3] J. Cao and G. A. Voth, J. Chem. Phys. **100**, 5106 (1994).

[4] I. R. Craig and D. E. Manolopoulos, J. Chem. Phys. **121**, 3368 (2004).

[5] J. A. Poulsen, G. Nyman, and P. J. Rossky, J. Chem. Phys. **119**, 12179 (2003).

[6] K. K. G. Smith, J. A. Poulsen, A. Cunsolo, and P. J. Rossky, J. Chem. Phys. **140**, 034501 (2014).

[7] M. Celli, U. Bafile, D. Colognesi, A. De Francesco, F. Formisano, E. Guarini, M. Neumann, and M. Zoppi, Phys. Rev. B **84**, 140510R (2011).

[8] U. Bafile, M. Celli, D. Colognesi, M. Zoppi, E. Guarini, A. De Francesco, F. Formisano, and M. Neumann, J. Phys.: Conf. Ser. **340**, 012076 (2012).

[9] P. Clark Souers, *Hydrogen Properties for Fusion Energy* (University of California Press, Berkeley, 1986).

[10] J. A. Young and J. U. Koppel, Phys. Rev. **135**, A603 (1964); V. F. Sears, Can. J. Phys. **44**, 1279 (1979).

[11] A. Rahman, K. S. Singwi, and A. Sjölander, Phys. Rev. **126**, 986 (1962).

[12] K. Sköld, J. M. Rowe, G. Ostrowski, and P. D. Randolph, Phys. Rev. A **6**, 1107 (1972).

[13] D. Colognesi, M. Celli, M. Neumann, and M. Zoppi, Phys. Rev. E **70**, 061202 (2004).

[14] G. Cicognani, H. Mutka, and F. Sacchetti, Physica B (Amsterdam) **276**, 83 (2000).

[15] G. Cicognani, H. Mutka, D. Weddle, B. Hamelin, Ph. Malbert, F. Sacchetti, C. Petrillo, and E. Babucci, Physica B (Amsterdam) **276**, 85 (2000).

[16] R. D. McCarty, J. Hord, and H. M. Roder, *Selected Properties of Hydrogen*, NBS Monograph 168 (NBS, Gaithersburg, MD, 1981).

[17] R. Prydz, The Thermodynamics Properties of Deuterium, National Bureau of Standards Reports 9276, Boulder Colo. 80303, 1967; H. M. Roder, G. E. Childs, R. D. McCarty, and P. E. Angerhofer, Survey of the Properties of Hydrogen Isotopes Below Their Critical Temperatures, National Bureau of Standards Technical Note 641 (U.S. Government Printing Office, Washington, D. C. 20402, 1973).

[18] M. Lambert, Phys. Rev. Lett. **4**, 555 (1960); H. F. P. Knaap, M. Knoester, and J. J. M. Beenakker, Physica (Amsterdam) **27**, 309 (1961); V. N. Grigor'ev and N. S. Rudenko, Zh. Eksp. Teor. Fiz. **40**, 757 (1961) [Sov. Phys.–JETP **13**, 530 (1961)]; N. G. Bereznyak, I. V. Bogoyavlenskiĭ, L. V. Karnatsevich, and A. A. Sheĭnina, Zh. Eksp. Teor. Fiz. **59**, 1534 (1970) [Sov. Phys.–JETP **32**, 838 (1971)].

[19] R. Treviño Arizpe, Rev. Mex. Fis. **4**, 23 (1955).

[20] S. W. Lovesey, *Theory of Neutron Scattering from Condensed Matter*, Vol. I (Oxford University Press, Oxford, 1987).

[21] S. Rols (private communication).

[22] W.-D. Seiffert, Measurement of Scattering Cross Sections of Liquid and Solid Hydrogen, Deuterium and Deuterium Hydride for Thermal Neutrons, Euratom Report No. EUR 4455d, 1970; W.-D. Seiffert, B. Weckermann, and R. Misenta, Z. Naturforsch. A **25**, 967 (1970).

[23] A. K. Agrawal, Phys. Rev. A **4**, 1560 (1971); V. F. Sears, Adv. Phys. **24**, 1 (1975).
[24] M. Zoppi, Physica B (Amsterdam) **183**, 235 (1993).
[25] P. A. Egelstaff and A. K. Soper, Mol. Phys. **40**, 553 (1980); P. Zetterström, A. K. Soper, and P. Schofield, *ibid.* **88**, 1621 (1996).
[26] V. F. Sears, Neutron News **3**, 29 (1992).
[27] J. Van Kranendonk, *Solid Hydrogen* (Plenum, New York, 1983).
[28] I. F. Silvera and V. V. Goldman, J. Chem. Phys. **69**, 4209 (1978).
[29] W. G. Hoover, *Computational Statistical Mechanics* (Elsevier, Amsterdam, 1991).
[30] W. H. Press, S. Teukolsky, W. T. Vetterling, and B. P. Flannery, *Numerical Recipes in Fortran 90. The Art of Parallel Scientific Computing* (Cambridge University Press, Cambridge, 1996).
[31] R. Kubo, Rep. Prog. Phys. **29**, 255 (1966).
[32] T. F. Miller III and D. E. Manolopoulos, J. Chem. Phys. **122**, 184503 (2005).
[33] K. Singer and W. Smith, Mol. Phys. **64**, 1215 (1988).
[34] M. F. Herman, E. J. Bruskin, and B. J. Berne, J. Chem. Phys. **76**, 5150 (1982).
[35] K. S. Singwi and M. P. Tosi, Phys. Rev. **149**, 70 (1966).
[36] U. Balucani and M. Zoppi, *Dynamics in the Liquid State* (Clarendon Press, Oxford, 1994).
[37] J. K. Krause and C. A. Swenson, Phys. Rev. B **21**, 2533 (1980); M. Zoppi, D. Colognesi, and M. Celli, Eur. Phys. J. B **23**, 171 (2001).
[38] J. P. Boon and S. Yip, *Molecular Hydrodynamics* (McGraw-Hill, New York, 1980).
[39] D. E. O'Reilly and M. Peterson, J. Chem. Phys. **66**, 934 (1977).
[40] F. Fernandez-Alonso, F. J. Bermejo, C. Cabrillo, R. O. Loutfy, V. Leon, and M. L. Saboungi, Phys. Rev. Lett. **98**, 215503 (2007).
[41] F. Fernandez-Alonso, C. Cabrillo, R. Fernàndez-Perea, F. J. Bermejo, M. A. Gonzàlez, C. Mondelli, and E. Farhi, Phys. Rev. B **86**, 144524 (2012).
[42] C. Andreani, D. Colognesi, J. Mayers, G. F. Reiter, and R. Senesi, Adv. Phys. **54**, 377 (2005).
[43] W. Langel, D. L. Price, R. O. Simmons, and P. E. Sokol, Phys. Rev. B **38**, 11275 (1988); K. W. Herwig, J. L. Gavilano, M. C. Schmidt, and R. O. Simmons, *ibid.* **41**, 96 (1990); F. J. Mompeán, M. García-Hernández, F. J. Bermejo, and S. M. Bennington, *ibid.* **54**, 970 (1996); C. Andreani, D. Colognesi, A. Filabozzi, M. Nardone, and R. T. Azuah, Europhys. Lett. **37**, 329 (1997).
[44] G. Watson, J. Phys: Condens. Matter **8**, 59 (1996).
[45] J. Dawidowski, F. J. Bermejo, M. L. Ristig, C. Cabrillo, and S. M. Bennington, Phys. Rev. B **73**, 144203 (2006).
[46] B. R. A. Nijboer and A. Rahman, Physica (Amsterdam) **32**, 415 (1966).
[47] D. Colognesi, U. Bafile, M. Celli, and M. Neumann, Chem. Phys. **446**, 57 (2015).
[48] T. Tsang, Phys. Rev A **17**, 393 (1978).
[49] B. J. Berne, J. Stat. Phys. **43**, 911 (1986).
[50] P. A. Egelstaff and P. Schofield, Nucl. Sci. Eng. **12**, 260 (1962).
[51] R. K. Shukla, S. K. Shukla, V. K. Pandey, and P. Awasthi, Phys. Chem. Liq. **45**, 169 (2007).